PROCESSING ISSUES IN THE DEVELOPMENT OF INDIUM-ARSENIDE-BASE HETEROJUNCTION BIPOLAR TRANSISTORS

A Thesis

Submitted to the Graduate School
of the University of Notre Dame
in Partial Fulfillment of the Requirements
for the Degree of

Master of Science in Electrical Engineering

by

Surajit K. Sutar, B.E.

____

Alan C. Seabaugh, Director

Department of Electrical Engineering
Notre Dame, Indiana

April 2003

PROCESSING ISSUES IN THE DEVELOPMENT OF INDIUM-ARSENIDE-BASE HETEROJUNCTION BIPOLAR TRANSISTORS

Abstract

by

Surajit K. Sutar

The issues in the fabrication of InAs based heterojunction bipolar transistors (HBT) have been discussed. The feasibility for using selective etchants in the process of defining the device mesas has been examined. Of the five etchants studied for selective etching of InAsP over InAs, the phosphoric acid based etchant etches InAsP faster than InAs with selectivity less than 2. A process for molybdenum contact formation on InAs has been developed including etching processes for molybdenum. Of the molybdenum etchants studied, three etchants have been found to be useful for the purpose, (a) H_2O_2 (etch rate 2.7 nm/s), (b) 15 NH_4OH: 10 H_2O_2: 100 H_2O (2.7 nm/s), and (c) reactive ion etching in CF_4/O_2 (1.9 nm/s). Employing this metallization process, molybdenum contacts have been made to undoped InAs and the metal contacts have been characterized by the transmission line method (TLM) measurement. Using the same metallization process, molybdenum contacts have been put on a *p-n* junction structure structurally identical to the base-collector junction of an HBT. The current-voltage characteristics and their dependence on annealing for the diodes have been studied. The lowest value of the ideality factor for the diodes measured has been found to be 1.25.

CONTENTS

TABLES iv

FIGURES v

ACKNOWLEDGMENTS vii

CHAPTER 1: INTRODUCTION AND MOTIVATION 1

CHAPTER 2: PRINCIPLE OF OPERATION OF THE HETEROJUNCTION BIPOLAR TRANSISTOR 5
2.1 The operation of a bipolar junction transistor 5
2.2 Bipolar transistor performance measures 7
2.3 Heterojunction bipolar transistor 10

CHAPTER 3: INDIUM ARSENIDE ETCHANTS AND SELECTIVE ETCHANTS 13
3.1 Sample preparation and measurement 14
3.2 $InAs_{0.78}P_{0.22}$/InAs etchants 15
3.2.1 Citric acid ($C_6H_8O_7.H_2O$) based etchant 15
3.2.2 1 H_3PO_4: 3 HCl 16
3.2.3 20 H_2O: 1 HBr: 1 H_2O_2 17
3.2.4 1 HBr: 1 CH_3COOH: 5 H_2O 18
3.2.5 1 HBr: 1 H_3PO_4: 5 H_2O 18

CHAPTER 4: REFRACTORY METAL CONTACTS STUDY 19
4.1 Non-lift-off metallization process 19
4.2 Preparation of molybdenum samples for etching 21
4.3 Etchants studied 21
4.3.1 HF based etchants 21
4.3.2 1 HNO_3: 1 H_2SO_4: 3 H_2O 22
4.3.3 1 HNO_3: 10 H_2O 23
4.3.4 1 HNO_3: 1 HCl: 1 H_2O 23
4.3.5 H_2O_2 24
4.3.6 15 NH_4OH: 10 H_2O_2: 100 H_2O_2 26
4.4 Photoresist-molybdenum adhesion issues 27

CHAPTER 5: MOLYBDENUM CONTACT CHARACTERIZATION 31
5.1 Transmission line method 31
5.2 Sample preparation and measurement 35

CHAPTER 6: BASE-COLLECTOR *P-N* JUNCTION STUDY 43
6.1 Diode parameters 43
6.2 Wafer structure and fabrication process 45
6.3 Current-voltage (I-V) characteristics and analysis 47
6.4 Effect of annealing on the current-voltage characteristics 53

CHAPTER 7: CONCLUSION 56

APPENDIX: PROCESS TRAVELLER FOR INDIUM ARSENIDE *P-N* DIODE WITH MOLYBDENUM CONTACT 57

REFERENCES 60

TABLES

4.1 Results of etching of electron-beam evaporated molybdenum films by HF based etchants……………………………………………………………………23

6.1 Diode parameters for the *p-n* structure device (wafer no. R315) with molybdenum contact to the *p*+ layer……………………………………………49

6.2 Current densities and the surface electron density at different applied bias …….53

FIGURES

1.1 Simulated current gain cut-off frequencies and power gain cut-off frequencies, f_T and f_{max}, respectively, as a function of base-emitter bias [2] based on an analytic model [4]. 2

2.1 (a) Schematic diagram of an *n-p-n* bipolar transistor connected under active mode bias. (b) Energy band diagram of an *n-p-n* InAs bipolar junction transistor with N_{dE} = 2 x 10^{17}, N_{aB} = 1 x 10^{19}, N_{dC} = 5 x 10^{16} cm^{-3}, V_{BE} = 0.2, V_{CB} = 0.5 V (using the Poisson solver BandProf program of W. R. Frensley) 6

2.2 Energy band diagram of an $InAs_{.78}$ $P_{0.22}$-InAs *n-p* heterojunction with N_d =2 x10^{17} and N_a = 1 x 10^{19} cm^{-3} at equilibrium (using D. W. Winston's SimWindows program). 11

3.1 Heterojunction bipolar transistor structure. 14

3.2 Layer diagram of $InAs_{0.78}P_{0.22}$-InAs heterojunction structure for selective etching study, wafer PEDI-90, grown by molecular beam epitaxy at HRL Laboratories, Malibu, Ca, ... 15

3.3 Citric acid based etch of $InAs_{0.78}P_{0.22}$ and InAs 16

3.4 3 HCl: 1 H_3PO_4 etch of $InAs_{0.78}P_{0.22}$ and InAs. 17

3.5 HBr: H_2O_2 etch of $InAs_{0.78}P_{0.22}$ and InAs. 18

4.1 Temperature variations in the Airco/Temescal FC-1800 electron-beam evaporation chamber during the deposition of molybdenum. 20

4.2 Molybdenum etching by H_2O_2. 24

4.3 Molybdenum etching by 15 NH_4OH: 10 H_2O_2: 100 H_2O 26

4.4 Etched molybdenum patterns after etching with H_2O_2, (a) photoresist hardbaked at 120 ºC for 1 minute with hexamethyldisilazane applied before photoresist, (b) photoresist hardbaked at 110 ºC for 4 minutes with hexamethyldisilazane applied

before photoresist, (c) photoresist hardbaked at 120 ºC for 2 minutes without the application of hexamethyldisilazane before photoresist. 28

4.5 Reactive ion etching of molybdenum in CF_4/O_2 plasma. 30

5.1 Transmission line method measurement configuration. 32

5.2 Electrical equivalent of the transmission line measurement set up 33

5.3 Resistance vs. contact spacing, *L*, in the transmission line method......................... 34

5.4 Total resistance vs. gap length for an unannealed molybdenum-InAs contact......... 37

5.5 Total resistance vs. gap length for molybdenum-InAs contact (after annealing). 38

5.6 Total resistance vs. gap length for an unannealed molybdenum-InAs contact with Ti/Pt/Au on top of molybdenum... 41

5.7 Total resistance vs. gap length for an unannealed molybdenum-InAs contact with Ti/Pt/Au on top of molybdenum. 42

6.1 *P-N* diode structure R315 grown by molecular beam epitaxy at Georgia Tech., Atlanta: (a) layer structure, (b) equilibrium energy band diagram (using the Poisson solver BandProf of W. R. Frensley).. 46

6.2 Structure of a device made from the *p*-n diode structure R315. 47

6.3 Current-voltage (*I-V*) characteristics for the *p-n* structure devices (wafer R315) with molybdenum contact to the *p*+ layer.. 48

6. 4 (a) Dependence of the total current on the device diameter for the *p-n* structure devices (wafer R315) with molybdenum contact to the *p*+ layer, (b) Energy band diagram at equilibrium for InAs (*p*-type N_a= 10^{19} cm^{-3}) showing the Fermi level pinning at the surface (using the Poisson solver Bandprof program of W. R. Frensley). 52

6. 5 Effect of annealing on the current-voltage (*I-V*) characteristics of the *p-n* diode structure (wafer R315) with molybdenum contact to the *p*+ layer. 54

6.6 Scanning electron microscope images of the *p-n* diode structure (wafer R315) after annealing, (a) an unprobed device, (b) a probed device having non-rectifying current-voltage (*I-V*) characteristics. 55

ACKNOWLEDGMENTS

I would like to express my sincere gratitude to my advisor Dr. Alan Seabaugh for his constant guidance and encouragement throughout the course of my study and research at the University of Notre Dame.

I am grateful to Dr. D. H. Chow of HRL Laboratories, Malibu, CA for his helpful insight and advice. I would like to thank my colleagues Bin Wu, Sajid Kabeer, Rajkumar Sankaralingam, Subhash Pidaparthi, and Qingmin Liu for their interest and help.

I would also like to thank Dr. Patrick J. Fay and Dr. Lars E. Wernerson for their guidance in my research and for their consent to be on the committee.

CHAPTER 1

INTRODUCTION AND MOTIVATION

Since its invention in 1947, the bipolar junction transistor (BJT), has had an enormous impact on the electronic industry and has accounted for a significant portion of research in solid state electronics. In the development of the bipolar transistors, one major breakthrough has been the invention of the heterojunction bipolar transistor (HBT), which is a BJT having heterojunctions in the device structure. In the HBT, through advanced epitaxial and processing technology, band gap differences between semiconductor materials are exploited to improve the performance of the device. The speed of BJTs can be increased by incorporating heterojunctions as the emitter-base junction. Heterojunction bipolar transistors also have high current drive capability. The high speed and high current drive capabilities of the HBT make it a popular choice in high speed circuits and high current drive applications like power amplifiers.

The performance of an HBT is dependent on a variety of factors including the semiconductor material, device geometry and contact properties. The high electron mobility of InAs, 3.3×10^{4} cm^2/Vs at 300 K [1], narrow energy bandgap, 0.354 eV at 300 K [1] combined with the wider gap InAsP as an emitter appears promising for circuits operating at high frequency and low power supply voltage. Of all the III-V binary semiconductors, InAs has the second lowest electron effective mass, $m^* = 0.023m_0$, at the

Brillouin zone center [1] (InSb has the lowest m^*). The high electron mobility in InAs reduces the base transit time, τ_B, of the HBT, thereby increasing the current gain cut-off frequency f_T. The required bias for the operation of the InAs HBT is also low, approximately 0.3 V. The low value of V_{BE} and the low V_{CE} mean that the supply voltage can be reduced, lowering the power dissipation.

Figure 1.1 shows a simulation [2] which compares the frequency response of HBTs of identical geometry, but different material systems. The Si/SiGe simulation results are in good agreement with recent measurements reported by IBM Microelectronics [3]. From Fig. 1.1, it's seen that the current gain cut-off frequency f_T, and power gain cut-off frequency, f_{max}, in the case of the InAsP/InAs HBT should at least be as high as the Si/SiGe system at about one-third of the emitter/base bias. If the circuit power supplies for InAs technology can be reduced by the same one-third, the power dissipation can be reduced by nearly a factor of ten.

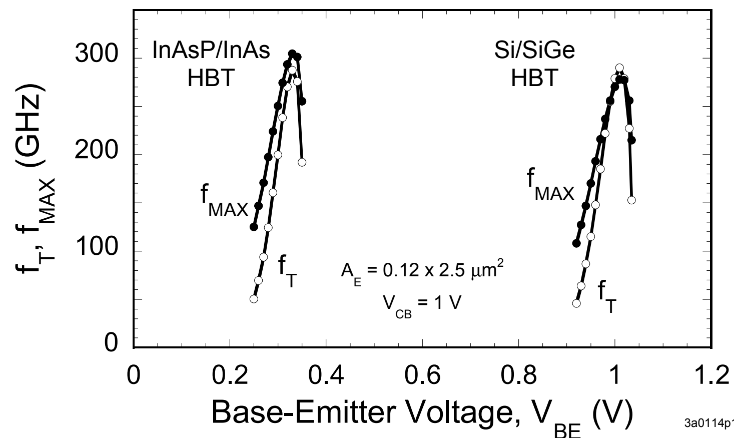

Fig. 1.1 Simulated current gain cut-off frequencies and power gain cut-off frequencies, f_T and f_{max}, respectively, as a function of base-emitter bias [2] based on an analytic model [4].

A discussion of the physics of the heterojunction bipolar transistor is given in Chapter 2. Development of any new technology offers numerous challenges. Apart from the issues involved in the growth of the proposed InAs HBT structure, a reliable process for the fabrication of the device is needed. For a vertical device like the HBT, an etching process is required to define the emitter, base and collector mesas.

The choice of a particular etching process is dependent upon many factors like the device structure and the mask set used. In a self-aligned process, some undercutting for the emitter and base mesas created by etching can be used for the isolation of the contact metals. With a structure having layers of different compositions, selective etchants for different layers are preferable. Chapter 3 deals with the study of selective etchants for InAsP over InAs.

A leakage current is sometimes observed in the current-voltage characteristics of a vertical InAs *p-n* junction, and one possible explanation for this could be surface conduction on the mesa sidewall [5]. One method to eliminate this leakage current is through the passivation of the base-collector mesa sidewall. To allow for the use of a wide temperature range in the exploration of base-collector passivation processes, a molybdenum-InAs contact has been developed, molybdenum being selected because of its refractory properties. Chapter 4 details the results obtained in the deposition and etching of molybdenum.

The transmission-line method was employed to characterize the molybdenum-InAs contacts. Chapter 5 describes the method and provides discussion. Finally, *p-n* diodes structurally similar to the base-collector junctions of an HBT were fabricated and analyzed. Chapter 6 discusses the current-voltage (*I-V*) characteristics of the fabricated

diodes. The diodes were also annealed at temperatures up to 200 ºC to explore the dependence of the current-voltage (*I-V*) characteristics on annealing.

CHAPTER 2

PRINCIPLE OF OPERATION OF THE HETEROJUNCTION BIPOLAR TRANSISTOR

A heterojunction bipolar transistor incorporates a heterojunction typically at the emitter-base junction to block the back injection of majority carriers in the base into the emitter. The blocking of back injection into the emitter allows for a higher base doping, resulting in better frequency performance, without compromising the current gain. To fully appreciate the operation of a HBT, it is necessary to first understand the operation of a BJT.

2.1 The operation of a bipolar junction transistor

Figure 2.1(a) shows an *n-p-n* transistor working in the active mode, i.e. the emitter-base junction forward biased and the base-collector junction reverse biased. The corresponding band diagram is shown in Fig. 2.1b. Because of the forward bias of the emitter-base junction, there is an injection of electrons from the emitter into the base and of holes from the base into the emitter region. The base width, W_B, is designed to be shorter than the diffusion length, L_B, of the electrons in the base region, which means that on average, an electron injected from the emitter will reach the base-collector junction before it recombines with a hole in the base. Said another way, the transit time, τ_B, of the electron is less than the electron lifetime, τ_n, in the base. Since the base-collector junction

is reverse biased, electrons reaching the base-collector depletion region are accelerated by the depletion region electric field into the collector.

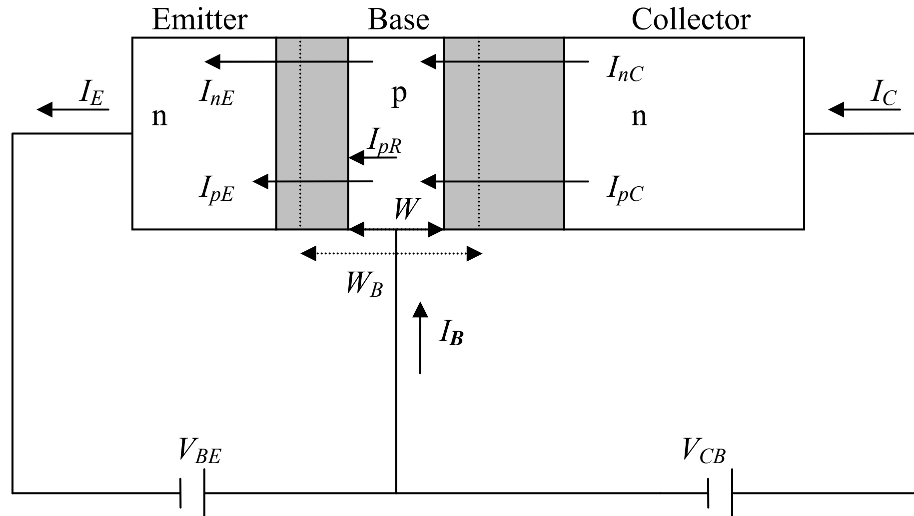

(a)

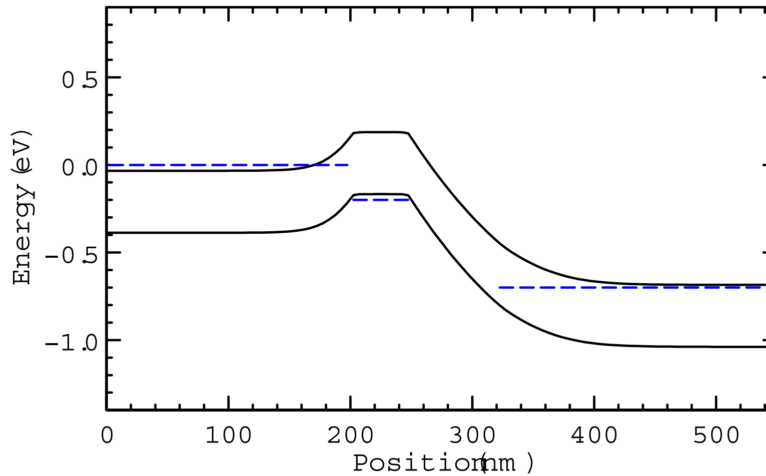

(b)

Fig. 2.1 (a) Schematic diagram of an *n-p-n* bipolar transistor connected under active mode bias. (b) Energy band diagram of an *n-p-n* InAs bipolar junction transistor with N_{dE} = 2 x 10^{17}, N_{aB} = 1 x 10^{19}, N_{dC} = 5 x 10^{16} cm^{-3}, V_{BE} = 0.2, V_{CB} = 0.5 V (using the Poisson solver BandProf program of W. R. Frensley).

2.2 Bipolar transistor performance measures

Referring to Fig. 2.1(a), the emitter current consists of two components: (a) the current due to electron injection into the base, I_{nE}, and (b) the current due to the injection of holes into the emitter from the base, I_{pE}. The base current, I_B, has three components: I_{pE}, due to hole injection into the emitter, I_{pR}, due to electron-hole recombination in the base, and I_{pC}, the current due to the hole generation in the base-collector junction. The collector current, I_C, consists of the emitter-injected electron current, I_{nC}, plus the current due to the generation in the base-collector junction, I_{pC}. In the configuration shown in Fig. 2.1(a), I_C equals the sum of I_B and I_E. The difference in I_{nE} and I_{pR} is equal to I_{nC}.

In the common-base configuration, the current gain is characterized by α, the common–base current gain, defined as [6],

$$\alpha = \frac{\partial I_C}{\partial I_E} = \frac{\partial I_{nE}}{\partial I_E}\frac{\partial I_{nC}}{\partial I_{nE}}\frac{\partial I_C}{\partial I_{nC}} \ . \tag{2.1}$$

The term $\frac{\partial I_{nE}}{\partial I_E}$ is called the emitter efficiency, γ, $\frac{\partial I_{nC}}{\partial I_{nE}}$ is defined as the base transport factor, α_T, and the term $\frac{\partial I_C}{\partial I_{nC}}$ is called the collector multiplication factor M so that Eq. (2.1) can be written

$$\alpha = \gamma \alpha_T M \ . \tag{2.2}$$

If the base-collector bias is low, i.e. less than required for impact ionization, M is approximately one.

The base transport factor α_T can be written [7]

$$\alpha_T = \frac{1}{\cosh\left(W/L_B\right)} \approx 1 - \frac{W^2}{2L_B^2} \ , \tag{2.3}$$

where W is the effective width of the base, see Fig. 2.1. If $W << L_B$, the value of α_T approaches unity. In fact, for bipolar transistors with W_B less than $1/10^{th}$ of the diffusion length, $\alpha_T > 0.995$ [7]. Taking $\alpha_T \sim 1$ (and $M \sim 1$), Eq. (2.2) becomes

$$\alpha = \gamma \, . \tag{2.4}$$

As defined earlier, the emitter efficiency γ is the ratio of incremental emitter-electron current to the incremental total emitter current, and increases with the decrease in the hole component of the emitter current. A high value of the emitter to base doping ratio gives a high γ, because of the reduction in the hole component in the total emitter current. In the common-emitter configuration, the current gain is given by the parameter β, called the common-emitter current gain,

$$\beta = \frac{\partial I_C}{\partial I_B} = \frac{\alpha}{1-\alpha} \ . \tag{2.5}$$

Assuming $\alpha_T \sim 1$, and $M \sim 1$, β can be written [7]

$$\beta \propto \frac{n_B}{p_E}\left(\frac{1}{W}\right) \ , \tag{2.6}$$

where, n_B is the electron density in the base and p_E is the hole density in the emitter.

Taking $p_E = \frac{n_i^2}{N_{dE}}$ and $n_B = \frac{n_i^2}{N_{aB}}$ (neglecting bandgap narrowing due to doping), Eq. (2.6) becomes

$$\beta \propto \frac{N_{dE}}{N_{aB} W} \ , \tag{2.7}$$

where N_{dE} is the emitter doping, N_{aB} is the base doping, and n_i is the intrinsic carrier concentration.

The frequency performance of a BJT is characterized by two parameters, the current gain cut-off frequency, f_T, and the maximum frequency of oscillation, f_{max}. The cut-off frequency, f_T, is defined as the frequency at which the common-emitter short-circuit current gain, β, is unity, and in the case of a BJT, can be written as [8]

$$f_T = \frac{1}{2\pi\tau_{EC}}, \tag{2.8}$$

where, τ_{EC} is the emitter-collector delay time, and can be written as the sum of four quantities:

$$\tau_{EC} = \tau_E + \tau_B + \tau_{dC} + \tau_C , \tag{2.9}$$

where τ_E is the emitter junction charging time, τ_B is the base transit time, τ_{dC} is the collector-base depletion layer transit time, and τ_C is the collector junction charging time. The base transit time τ_B is can be expressed in terms of the base width as [9]

$$\tau_B = \frac{W^2}{2D_{nB}} , \tag{2.10}$$

where D_{nB} is the diffusion constant of the electrons in the base.

Equation (2.10) shows that the base transit time varies as the square of the base width. So reduction of the base width can significantly affect the base transit time and hence the cut-off frequency.

The frequency f_{max}, at which the unilateral power gain of the transistor becomes unity, can be expressed in terms of the cut-off frequency [10]

$$f_{\max} = \sqrt{\frac{f_T}{8\pi r_b C_C}}, \tag{2.11}$$

where r_b is the base resistance, and C_C is the collector-base junction capacitance.

2.3 Heterojunction bipolar transistor

From Eq. (2.7), it is seen that to achieve high values of β in the BJT, the ratio of the emitter to base doping is maximized. However, a low base doping density results in a high base resistance, r_b, and a larger base resistance decreases f_{max}, see Eq. (2.11). Using a heterojunction at the emitter-base junction, a potential barrier can be presented for the majority carriers in the base, thus limiting the injection current into the emitter. This way, higher doping can be allowed in base giving a low r_b, but at the same time, giving a high β.

Figure 2.2 shows the band diagram for the $InAs_{0.78}P_{0.22}$/InAs emitter-base abrupt heterojunction. As seen in Fig. 2.2, the transition of the material composition between the emitter and base (from InAsP to InAs) is abrupt, which gives a discontinuity in the edges of the band edges of the base and the emitter. From the band diagram, it can be seen that, the valence band discontinuity presents a barrier for the holes in the base injected into the emitter. This means that even if the hole concentration in the base is high because of high doping giving a low base resistance, the hole injection into the emitter can still be limited. This results in high emitter efficiency, γ, and thus a high current gain, β. At the same time, because of the low base resistance, a high f_{max} can be achieved.

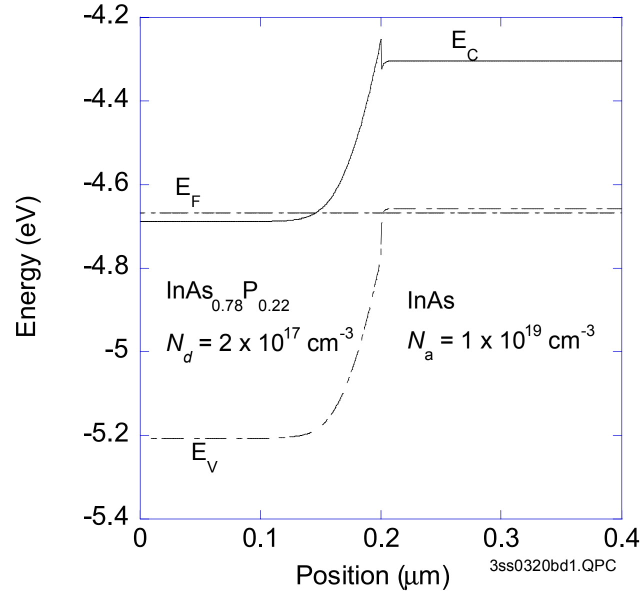

Fig. 2.2 Energy band diagram of an $InAs_{.78}$ $P_{0.22}$-InAs *n-p* heterojunction with N_d =2 x10^{17} and N_a = 1 x 10^{19} cm^{-3} at equilibrium (using D. W. Winston's SimWindows program).

An estimate for the maximum value of β for the HBT can be made from the formula [11, 12]

$$\beta_{\max} = \frac{N_{dE} v_n}{N_{aB} v_p} e^{\Delta E_v / kT}, \tag{2.12}$$

where v_n and v_p are the mean electron and hole velocities due to the effects of both drift and diffusion and ΔE_V is the valence band discontinuity of the heterojunction. For an InAs heterojunction bipolar transistor, with an $InAs_{0.78}P_{0.22}$-InAs emitter-base heterojunction, typical values of N_{dE} and N_{aB} are 2×10^{17} and 1×10^{19} cm^{-3}, respectively. For an $InAs_{0.78}P_{0.22}$-InAs heterojunction, the values of ΔE_g , ΔE_C , and ΔE_V are 0.165,

0.0825, and 0.0825 eV, respectively [5]. For InAs, taking v_n/v_p~73 (as the ratio of electron and hole mobilities), β_{max} is estimated as ~36.

Using a heterojunction also provides improvements in frequency performance because of the lower electron transit time in the base. Because of the discontinuity in the conduction band edge ΔE_C in the case of an abrupt heterojunction, the electrons entering the base from the emitter region have their kinetic energy and thus their drift velocity increased in the base [13, 14]. If the base width is comparable to the electron mean free path in the base, then electrons can reach the base-collector region without suffering many collisions, so that their energies and velocities can exceed equilibrium values. This velocity overshoot effect can reduce the base transit time which increases the value of f_T and f_{max}.

In a vertical structure like the HBT, the effect of surface states along the mesa sidewall has to be taken into consideration. In InAs, Fermi level pinning by the surface states can create an accumulation layer of electrons along the surface [15]. Measurements show the Fermi level at the surface for InAs (110) is pinned such that the conduction band minimum at the surface is 0.189 to 0.199 eV below the Fermi level [16]. The formation of an accumulation layer leads to surface conduction. In the case of an HBT, surface conduction along the base-collector mesa has the effect of lowering the output resistance of the transistor and providing a C-B feedback path, which are undesirable. To eliminate the surface conduction, the formation of such an accumulation layer has to be prevented. This can be done through various surface passivation processes.

CHAPTER 3

INDIUM ARSENIDE ETCHANTS AND SELECTIVE ETCHANTS

A schematic diagram of a typical III-V HBT cross section is shown in Fig. 3.1. In the fabrication process, emitter, base, and collector mesas are defined by etching; photolithography and vacuum metal evaporation are used to define contacts. Since the base layer is thin, it is important to have control over the etching process as slight under-etching or over-etching of the emitter mesa could result in the base contact metal being displaced into the emitter or collector regions, respectively. Dry etching, if the etch mechanism is dominated by physical sputtering, is more anisotropic than wet etching. However with dry etching, there is a possibility of damage to the semiconductor surface and introduction of defects into the semiconductor. Wet etchants are easy to use and eliminate concern over defect creation. In this work, the focus has been on the development of wet etchants.

A selective etchant that etches the emitter layer but not the base layer is desirable. That way, the emitter can be over-etched to ensure the emitter layer is removed uniformly while leaving the base intact.

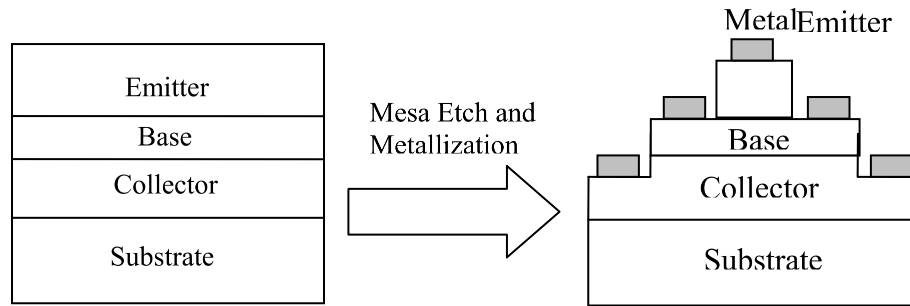

Fig. 3.1 Heterojunction bipolar transistor structure.

3.1 Sample preparation and measurement

The structure of an $InAs_{0.78}P_{0.22}$-InAs test heterojunction (wafer PEDI-90), grown by molecular beam epitaxy (MBE) at HRL Laboratories, is shown in Fig. 3.2. The structure has 90 nm of $InAs_{0.78}P_{0.22}$ on InAs. The composition of this test heterojunction is the same as in the emitter-base heterojunction for HBTs. The critical thickness, h_C, for this $InAs_{0.78}P_{0.22}$ layer is found to be 122 nm by the Matthews-Blakeslee model [17], which is higher than the 90 nm layer thickness, so the $InAs_{0.78}P_{0.22}$ layer is expected to be pseudomorphic. This sample was used for the calibration of InAsP etchants. A metal pattern (Ti/Pt/Au) was defined on the samples by photolithography and metallization. The metal pattern on the sample surface was step-profiled by a KLA Tencor Alpha-step-500 surface profiler for different etch times to get the metal height plus the etch depth. One piece of the wafer (1 cm × 1 cm) was used for one etching study. The sample was held vertically in a Teflon boat during etching. The etching was done at room temperature (without any temperature control) with some stirring. The surface was step-

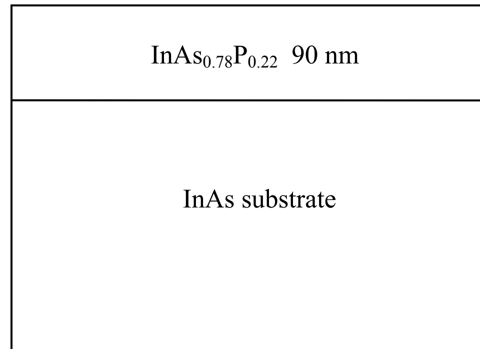

Fig. 3.2 Layer diagram of $InAs_{0.78}P_{0.22}$-InAs heterojunction structure for selective etching study, wafer PEDI-90, grown by molecular beam epitaxy at HRL Laboratories, Malibu, CA

profiled at several points on the surface for every etch depth. The multiple data points at each etch depth at a given etch time correspond to these measurements.

3.2 $InAs_{0.78}P_{0.22}$/InAs etchants

3.2.1 Citric acid ($C_6H_8O_7.H_2O$) based etchant

The citric acid based etchant is an industry proprietary etchant for InAs. The purpose of this study was to find out if it etches InAsP at a different rate than InAs. The result of this study is provided in Fig. 3.3. From Fig. 3.3, it can be seen that the etch rate for InAsP is lower than for InAs. The etch selectivity for InAs over InAsP is just above 2:1, which is not as high as would be ideal for a selective etching of an InAs emitter on an InAsP layer .

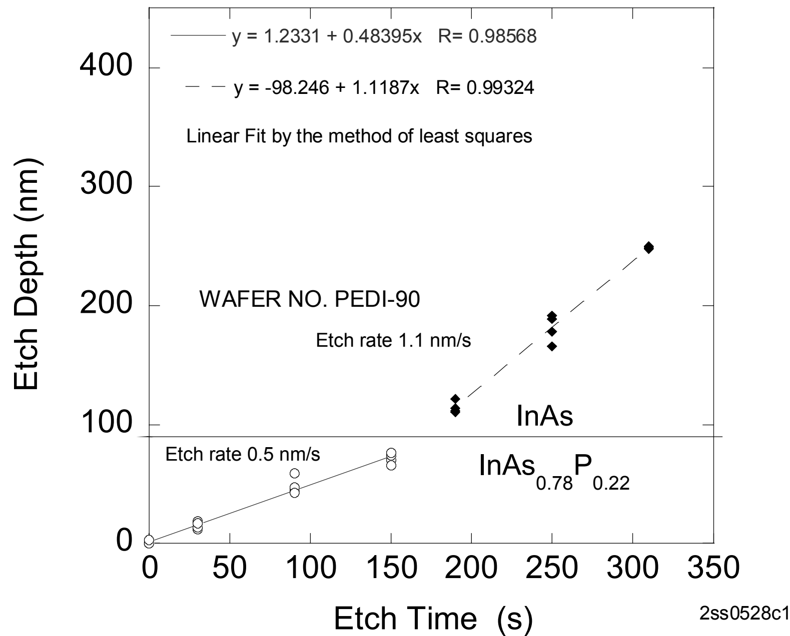

Fig. 3.3 Citric acid based etch of $InAs_{0.78}P_{0.22}$ and InAs

3.2.2 1 H_3PO_4: 3 HCl

Phosphoric acid (H_3PO_4) and hydrochloric acid (HCl) based etchants have been used to etch InP [18]. It is also reported [18] that InGaAs can be used as an etch mask for this etchant which means that it etches InGaAs at a very slow rate. So this etchant was studied to find out if it could be used to etch InAsP selectively over InAs. The InAsP on InAs sample (PEDI-90) was used for this study. The etch data is shown in Fig. 3.4. It can be seen that the etchant etches both InAs and InAsP at significant rates (1.1 and 0.5 nm/s, respectively). The etch rate is higher for $InAs_{0.78}P_{0.22}$, with a modest selectivity of 1.3:1 obtained for etching of $InAs_{0.78}P_{0.22}$ over InAs.

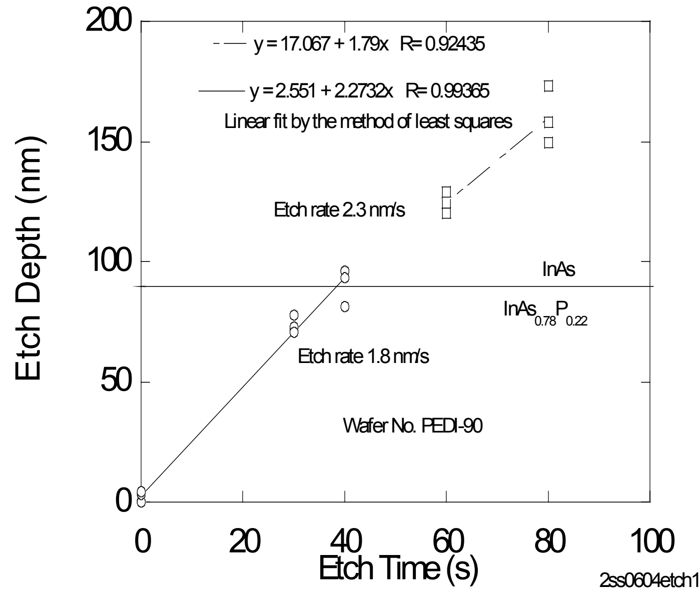

Fig. 3.4 3 HCl: 1 H_3PO_4 etch of $InAs_{0.78}P_{0.22}$ and InAs.

3.2.3 20 H_2O: 1 HBr: 1 H_2O_2

Solutions of HBr and H_2O_2 have been used to etch InP [19]. Since the InAsP layer in the HBT structures has significant phosphorous percentage (22 %), the feasibility of using this etchant was explored. The results are given in Fig. 3.5. As seen in Fig. 3.5, the etchant etches InAs at a faster rate (4.5 nm/s) than it etches InAsP (2.2 nm/s). So for the purposes of use as a selective etchant of InAsP over InAs, this etchant is not suitable.

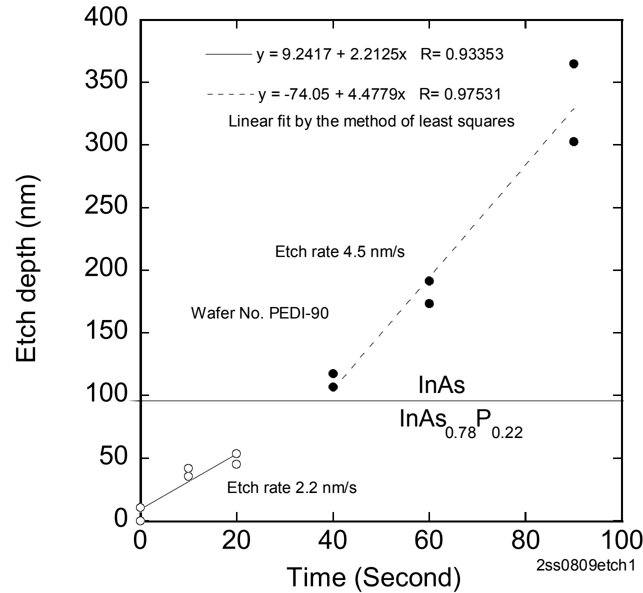

Fig. 3.5 HBr: H_2O_2 etch of $InAs_{0.78}P_{0.22}$ and InAs.

3.2.4 1 HBr: 1 CH_3COOH: 5 H_2O

Etching of InP by HBr: CH_3COOH solutions have been reported in [19] and [20]. Since the InAsP layer has a significant phosphorous content (22%), this etchant was tried on one piece of PEDI-90. After 3 minutes of soaking in the etchant (without stirring), no change in the etch depth was noticed.

3.2.5 1 HBr: 1 H_3PO_4: 5 H_2O

Etching of InP by HBr: H_3PO_4 systems has been reported [19, 20]. After 13 minutes of soaking in the etchant (without stirring), no change in the etch depth was observed, again using wafer PEDI-90. Therefore this etchant doesn't attack $InAs_{0.78}P_{0.22}$.

CHAPTER 4

REFRACTORY METAL CONTACTS STUDY

A refractory metal is defined as a metal having a melting point equal to or greater than that of chromium [21]. Out of the 12 such refractory metals (vanadium, niobium, tantalum, chromium, molybdenum, tungsten, rhenium, hafnium, ruthenium, rhodium, osmium and iridium) in the periodic table, molybdenum was selected primarily because of its availability. The reported values of the melting point of molybdenum are 2617 ºC [22], 2610 ºC [21] and 2620 ºC [23]. It has an electrical resistivity of 5.14 μΩ-cm [24] ([22] puts it at 5.2 μΩ-cm) at 273 K compared to 2.35 μΩ-cm for gold [22].

4.1 Non-lift-off metallization process

An Airco Temescal FC1800 electron-beam evaporator was used for molybdenum metallization. The yield of a lift-off process is sensitive to the baking conditions of the photoresist. The deformation of the photoresist baked at higher than optimum temperatures can give altered pattern dimensions after lift-off, and may result in the presence of metal flags along the edge of the pattern. The thermal deformation of the positive photoresist and a remedy by deep ultraviolet (UV) exposure of the photoresist has been reported [25]. All of these concerns can be circumvented by developing an etch process for wet chemically removing Mo over InAs. First, the variation of temperature of

the sample holder during molybdenum deposition is shown in Fig. 4.1. A thermocouple was placed in contact with a metallic sample holder inside an Airco Temescal evaporator, 1 cm away from the sample. The thermocouple was shielded from the evaporation source by the clip used to hold the thermocouple on the sample holder. Considering the possible time delays in the transfer of heat to the thermocouple, Fig. 4.1 gives an estimate of the lower limit for the temperature of the sample. From Fig. 4.1, it is seen that the temperature has a maximum value of 63 ºC. As discussed above, this value is a lower limit of the temperature of the sample and the sample could have been at a higher temperature.

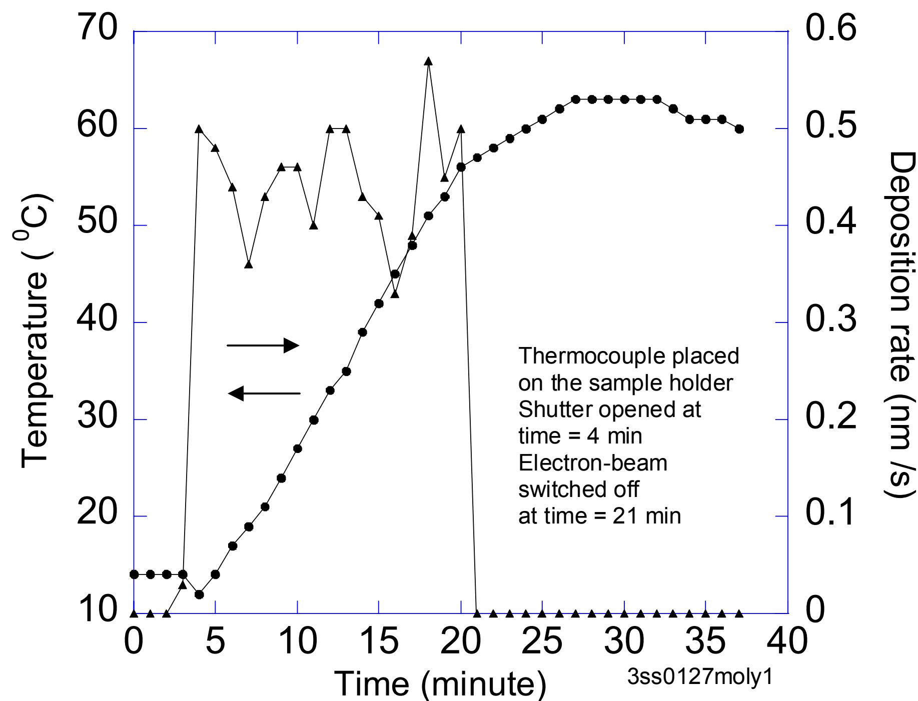

Fig. 4.1 Temperature variations in the Airco/Temescal FC-1800 electron-beam evaporation chamber during the deposition of molybdenum.

4.2 Preparation of molybdenum samples for etching

Etchants not likely to attack InAs were considered for this study. Before evaporation, the samples were cleaned by soaking in boiling acetone and methanol (5 minutes each). Using electron-beam evaporation, molybdenum (70-90 nm) was deposited on Si and InAs wafers. The electron-beam evaporation was done at a base pressure of 1.5×10^{-6} torr, the applied voltage and current for the source being 10 kV and 0.1 A, respectively. The wafers were patterned using AZ-5214E photoresist. Samples (5 mm × 5 mm) were then treated with the etchant and were step-profiled in a KLA Tencor Alpha-step surface profiler to get the etch depth after removing the photoresist. In the case of wet etching, the samples were held vertically in a Teflon boat. The wet etching was done at room temperature (without any temperature control) with stirring. For every measurement, multiple readings were obtained by step-profiling the surface at different places. The multiple values of the etch depth for etch time correspond to these readings. After etching, usually a brown oxide film (~20 nm, obtained from the difference in the etch depths before and after the removal of the film) is formed on the surface. This could be taken off by soaking in 1 HCl : 10 H_2O for 10 s.

4.3 Etchants studied

4.3.1 HF based etchants

The results for HF based etchants are summarized in Table 4.1. For x HF: y H_2O_2: z H_2O solutions, the surface of the sample after etching was rough (average surface roughness measured was as high as 319 nm). The places where maximum etch depth was measured were dark brown, and at other places the molybdenum film appeared to be

fragmented. Some samples were soaked in HCl (concentrated and diluted) to see if this would remove the brown film. Three hours of soaking in HCl didn't remove the film.

4.3.2 1 HNO_3: 1 H_2SO_4: 3 H_2O

The etchant removes approximately 80 nm molybdenum in 10 seconds. The etchant doesn't attack silicon. However, it attacks InAs rapidly (from both the top and back surfaces).

TABLE 4.1

RESULTS OF ETCHING OF ELECTRON-BEAM EVAPORATED MOLYBDENUM FILMS BY HF BASED ETCHANTS

No.	Etchant	Etch Time (s)	Etch Depth (nm)	Avg. Rough. (nm)	Etch Rate (nm/s)	Molybdenum etching notes
1	$1HF:1H_2O$	60	-	-	-	no etching
2	$1HF:5H_2O$	300	-	-	-	no etching
3	$1HF:2H_2O_2$	20	1240	-	62.0	nonuniform and rough
		30	2354	-	78.5	
4	$1HF:1H_2O_2$	20	76	-	3.8	nonuniform and rough
		40	92	-	2.3	
5	$1HF:1H_2O_2:1H_2O$	20	2	4	0.1	nonuniform and rough
		40	24	3	0.6	
		100	218	40	2.2	
		240	599	20	2.5	
6	$1HF:1H_2O_2:5H_2O$	120	6	3	0.0	nonuniform and rough
		300	45	61	0.2	
		600	1400	319	2.3	
7	$1HF:1H_2O_2:10H_2O$	900	1150	-	1.3	nonuniform and rough
8	$1HF:1H_2O_2:25H_2O$	1500	713	-	0.5	nonuniform and rough
9	$1HF:1H_2O_2:50H_2O$	1200	0	-	0.0	nonuniform and rough
10	$1HF:1H_2O_2:200H_2O$	5400	786	79	0.1	no Mo, test on Si substrate
		5400	5250	-	1.0	no Mo, test on InAs substrate
11	$1HF:2H_2O_2:5H_2O$	10	337	-	33.7	nonuniform and rough
12	$1HF:2H_2O_2:10H_2O$	10	211	-	21.1	nonuniform and rough

4.3.3 1 HNO_3: 10 H_2O

The Mo film was soaked in the etchant for 20 minutes without stirring. No etching was observed.

4.3.4 1 HNO_3: 1 HCl: 1 H_2O

This etchant attacks InAs rapidly (from the back surface), so it's not suitable for defining Mo contacts on InAs.

4.3.5 H_2O_2

The result is given in Fig. 4.2. The etching was done with Photoresist (5214E) as an etch mask, and it was observed that for longer etch times (greater than 3 minutes), the molybdenum under the photoresist was etched at the edges. It suggests adhesion problems between molybdenum and the photoresist or H_2O_2 attacking the photoresist.

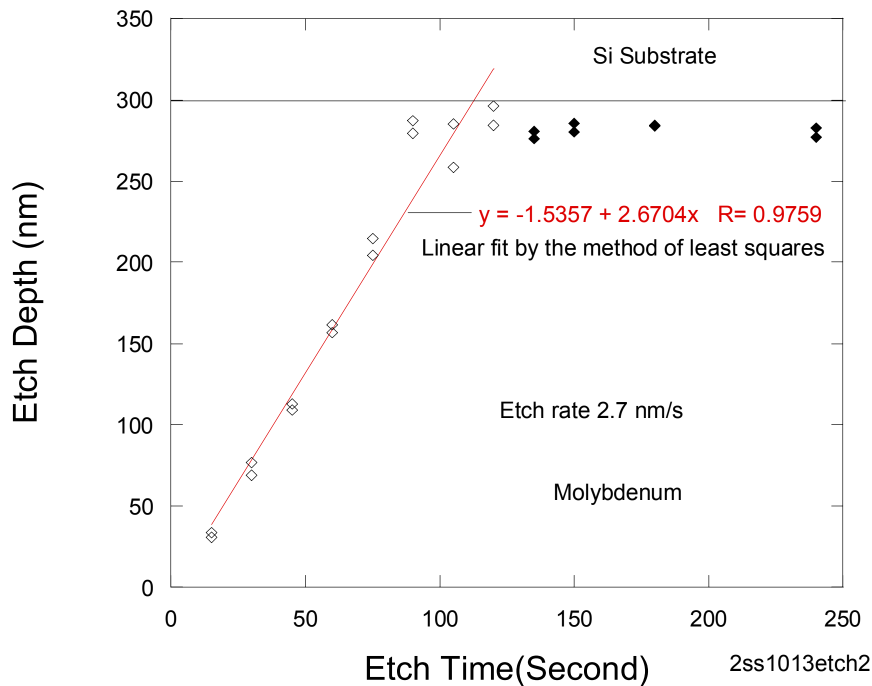

Fig. 4.2 Molybdenum etching by H_2O_2.

The following mechanism for the etching of molybdenum in a solution of hydrogen peroxide in water has been reported [26]:

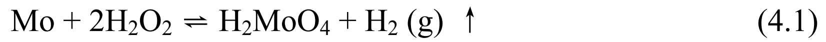

$$Mo + 2H_2O_2 \rightleftharpoons H_2MoO_4 + H_2\,(g) \uparrow \quad (4.1)$$

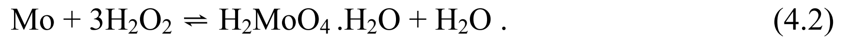

$$Mo + 3H_2O_2 \rightleftharpoons H_2MoO_4.H_2O + H_2O\,. \quad (4.2)$$

The other equilibria that might be present in the system are [26]:

$$MoO_4^{2-} + 2\,H_2O_2 \rightleftharpoons HMoO_6^{-} + OH^{-} + H_2O \quad (4.3)$$

$$MoO_4^{2-} + 4\,H_2O_2 \rightleftharpoons MoO_8^{2-} + OH^{-} + 4H_2O\,. \quad (4.4)$$

Eq. (4.1) and Eq. (4.2) give two products of the dissociation of molybdenum in the peroxide solution, H_2MoO_4 and $H_2MoO_4.H_2O$. The high oxidation degree of molybdenum (Mo^{+6}) is thermodynamically stable [26], so these two products are likely to be formed in the process of etching. The typical coloration of $HMoO_6^{-}$ and MoO_8^{2-} are pale yellow and red respectively [26]. The reaction rate is limited by the fact that the products of Eq. (4.1) and Eq. (4.2) are slightly soluble in water and passivate the Mo surface rapidly [26]. After 3 minutes; there were places where the photoresist (5214E) seemed to have been worn off at the edges of features. It suggests adhesion problems between molybdenum and the photoresist or the solution attacking the photoresist.

4.3.6 15 NH_4OH: 10 H_2O_2: 100 H_2O_2

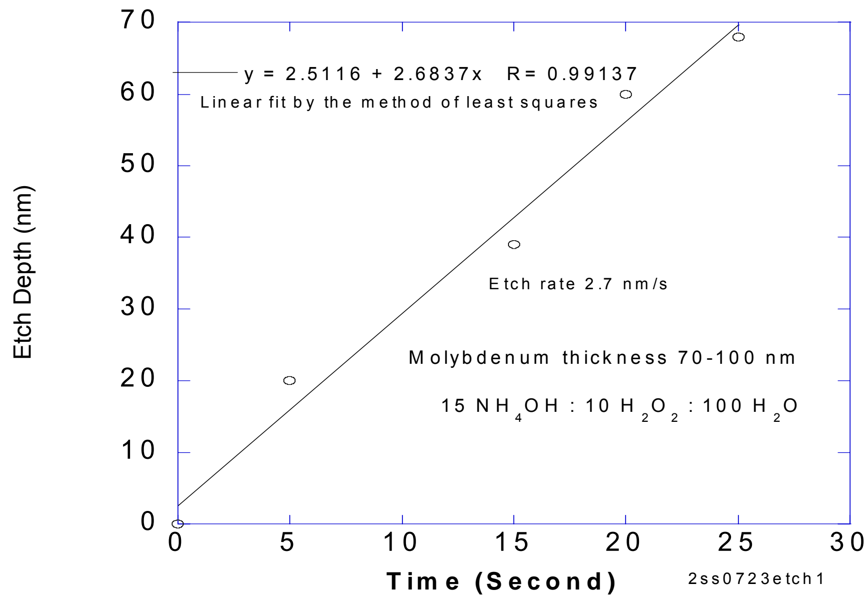

Fig. 4.3 Molybdenum etching by 15 NH_4OH: 10 H_2O_2: 100 H_2O.

The following mechanism for the etching of molybdenum in a solution of ammonium hydroxide and hydrogen peroxide in water has been reported [26]:

$$Mo + 2H_2O_2 + 2NH_3 \rightleftharpoons (NH_4)_2MoO_4 + H_2\,(g)\uparrow \qquad (4.5)$$

$$Mo + 3H_2O + 2NH_3 \rightleftharpoons (NH_4)_2MoO_4 + 2H_2O\,. \qquad (4.6)$$

Other reactions taking place in the system may be (along with Eq. (4.2), Eq. (4.3) and Eq. (4.4)) [26]:

$$NH_3 + H_2O \rightleftharpoons NH_4^+ + OH^- \qquad (4.7)$$

$$NH_3\,(l) \rightleftharpoons NH_3\,(g) \tag{4.8}$$

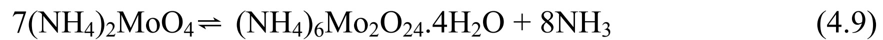

$$7(NH_4)_2MoO_4 \rightleftharpoons (NH_4)_6Mo_2O_{24}.4H_2O + 8NH_3 \tag{4.9}$$

$$H_2O_2 \rightleftharpoons H^+ + HO_2^- \tag{4.10}$$

$$H_2O \rightleftharpoons H^+ + OH^- . \tag{4.11}$$

The product $(NH_4)_2MoO_4$ in Eq. (4.5) and Eq. (4.6) represents the stable +6 oxidation state of molybdenum and is thus a likely product [26]. As discussed in 4.3.5, the products of Eq. (4.1) and Eq. (4.2) are only slightly soluble in water, and passivate the molybdenum surface. The product of Eq. (4.5) and Eq. (4.6) is highly soluble in water and thus would be rapidly separated from the molybdenum surface. So compared to pure peroxide etching, the ammonia-peroxide etching is likely to be less limited by the passivation of the molybdenum surface by insoluble reaction products. Equation 4.7 represents the ionization of the ammonia in water. Equation (4.8) represents the possible change in the NH_3 concentration of the solution due to the escape of NH_3 (g). Equation (4.9) represents the effect of the escape of ammonia from $(NH_4)_2MoO_4$ to form $(NH_4)_6Mo_2O_{24}.4H_2O$.

4.4 Photoresist-molybdenum adhesion issues

As mentioned in the sections describing molybdenum etching in H_2O_2 and NH_4OH: H_2O_2: H_2O, there seemed to be some etching underneath the photoresist (AZ5214E). The photoresist pattern after etching looked perfect but removing the photoresist revealed the etching on the metal underneath it. Weak adhesion between the photoresist and the molybdenum surface could be a reason for this. Some modifications

to the original photolithography process with regards to the baking conditions and application of adhesion promoters were done to circumvent this problem. The micrographs of the molybdenum patterns after etching and removing the photoresist for different conditions of lithography and baking are listed in Fig. 4.4. It is evident from Fig. 4.4 that the adhesion of AZ 5214E photoresist to molybdenum surface is better if hexamethyldisilazane (HMDS) is not applied before spinning the photoresist.

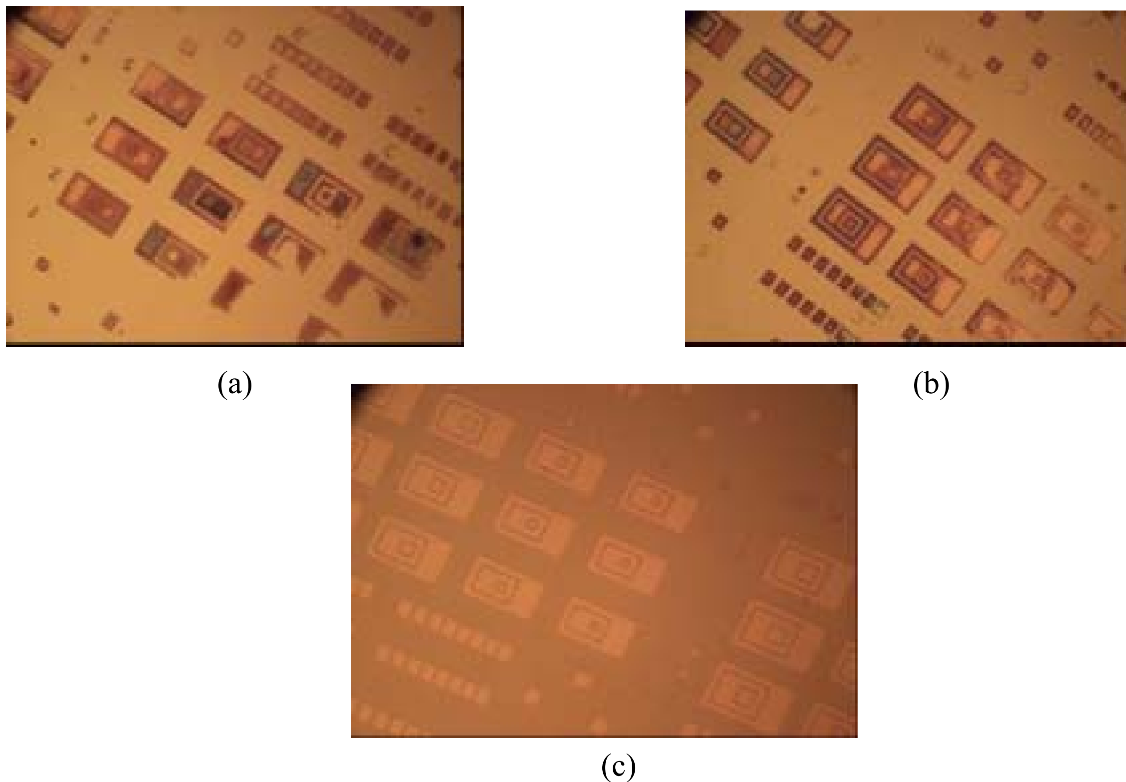

(a) (b) (c)

Fig. 4.4 Etched molybdenum patterns after etching with H_2O_2, (a) photoresist hardbaked at 120 ºC for 1 minute with hexamethyldisilazane applied before photoresist, (b) photoresist hardbaked at 110 ºC for 4 minutes with hexamethyldisilazane applied before photoresist, (c) photoresist hardbaked at 120 ºC for 2 minutes without the application of hexamethyldisilazane before photoresist.

To avoid this problem of adhesion altogether, the use of etch masks other than AZ5214E photoresist was considered. One such etch mask was SiO_2, deposited in a Unaxis-790 PECVD (plasma enhanced chemical vapor deposition) system. The metallization process was to: (a) deposit SiO_2 all over the molybdenum surface, (b) spin and pattern photoresist on the SiO_2 surface, (c) CF_4 and O_2 plasma RIE (reactive ion etch) the SiO_2, (d) remove the photoresist in acetone, (e) wet chemical etch the molybdenum to etch molybdenum, and (f) remove the SiO_2 mask in buffered HF.

It was found that the CF_4/O_2 plasma, apart from etching SiO_2, also etches molybdenum at a significant rate as shown in Fig. 4.5. That led to the idea of using the CF_4 and O_2 plasma as a dry etchant for molybdenum. The etch rate was found to be 1.9 nm/s from Fig. 4.5. The etchant doesn't attack InAs, but with a DC bias of ~ 200 V, it may introduce surface damage.

The etch has a chemical component to it in addition to sputtering. In the etching of molybdenum in fluorine based plasmas, the products formed are MoF_n and $MoOF_n$ [27].

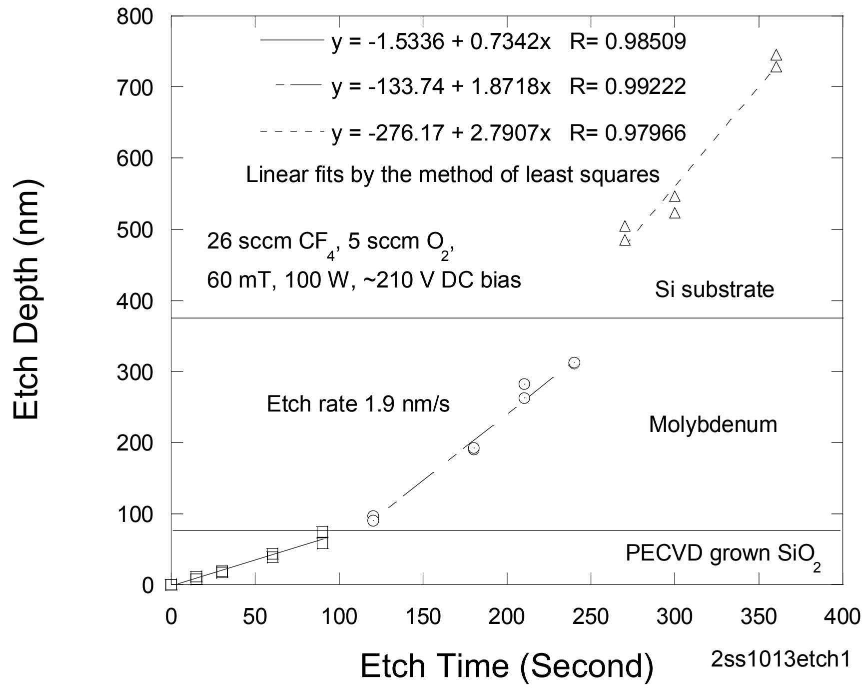

Fig. 4.5 Reactive ion etching of molybdenum in CF_4/O_2 plasma.

CHAPTER 5

MOLYBDENUM CONTACT CHARACTERIZATION

With the molybdenum metallization process in place, the electrical properties of the molybdenum-InAs interface were examined. The transmission line method (TLM) measurement was used to characterize the molybdenum-InAs contact.

5.1 Transmission line method

A common method to characterize ohmic contacts is the transmission line method (TLM), originally proposed by Shockley [28]. A schematic diagram of the measurement set up is given in Fig. 5.1. Rectangular metal pads of width W and length S are deposited on a mesa created on the semiconductor surface. The distance between these metal pads is set in increasing order ($L_1 < L_2$ and so on). A current source (I) and a voltmeter (V) are connected across two adjacent metal pads. The pads are deposited on a mesa so as to confine the current within the mesa width M_w. Electrically, the system can be represented as in Fig. 5.2.

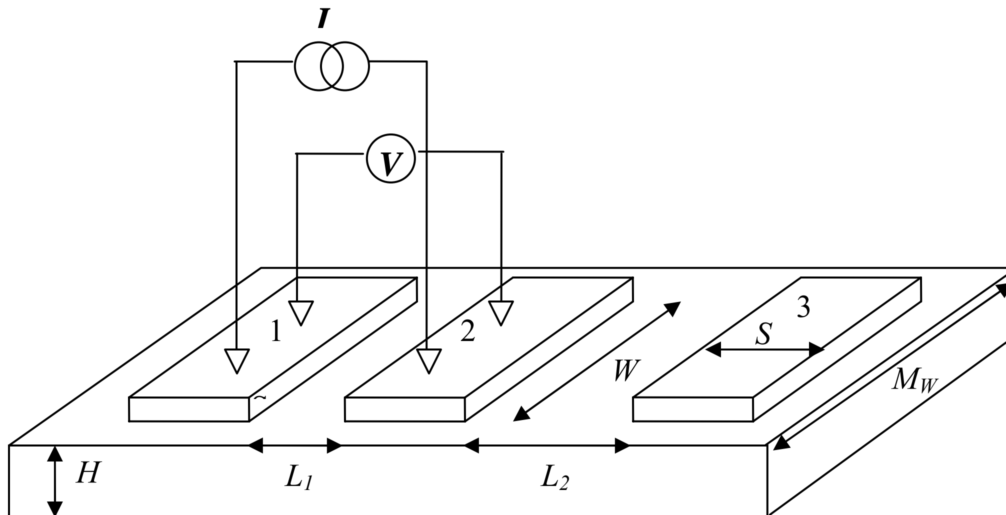

Fig. 5.1 Transmission line method measurement configuration.

Referring to Fig. (5.2), R_{PM} is the resistance between the probe and the metal pad, R_C is the contact resistance of the metal-semiconductor interface, R_S is the resistance due to the semiconductor, L is the distance between the metal pads, V is the voltage measured between the metal pads and I is the current supplied by the current source.

If it is assumed that the voltmeter resistance is much higher than $2R_C + R_S$, then it follows that negligible current will flow through the voltmeter, and the current (I) supplied by the current source (the measured value), will be the same as flowing through the R_C's and R_S. The voltage measured by the voltmeter, V, gives the potential difference between the metal pads. So the ratio (V/I) will give the value $2R_C + R_S$. Thus the probe to metal resistance, R_{PM}, is removed from the measurement. For accurate measurements, this is desirable because R_{PM} can vary with the probe quality and the probing pressure.

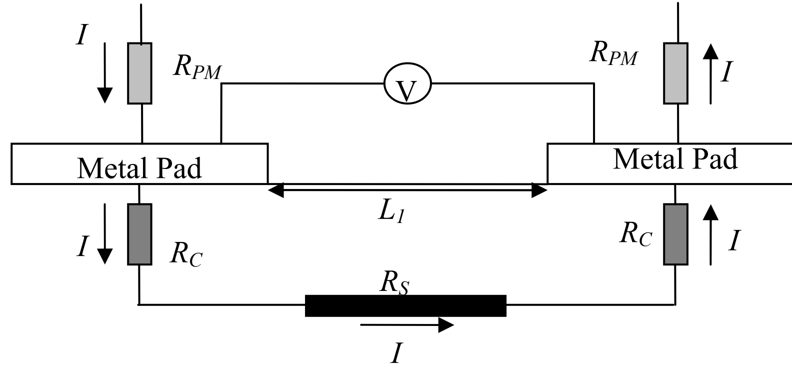

Fig. 5.2 Electrical equivalent of the transmission line measurement set up

If R_{SH} is the sheet resistance of the semiconductor, given as

$$R_{SH} = \rho / t \ . \tag{5.1}$$

Where ρ is the bulk resistivity of the semiconductor and t is the depth of the conducting semiconductor (in this case the mesa height),

$$R_S = (R_{SH}/W)L \ . \tag{5.2}$$

so that

$$R_{Total} = 2R_C + R_S \ .$$

$$=2R_C+(R_{SH}/W)L \ . \tag{5.3}$$

If the total resistance $R_{Total}\left(=\dfrac{V}{I}\right)$ is plotted as a function of the spacing L between the metal pads, it gives a straight line as shown in Fig. 5.3.

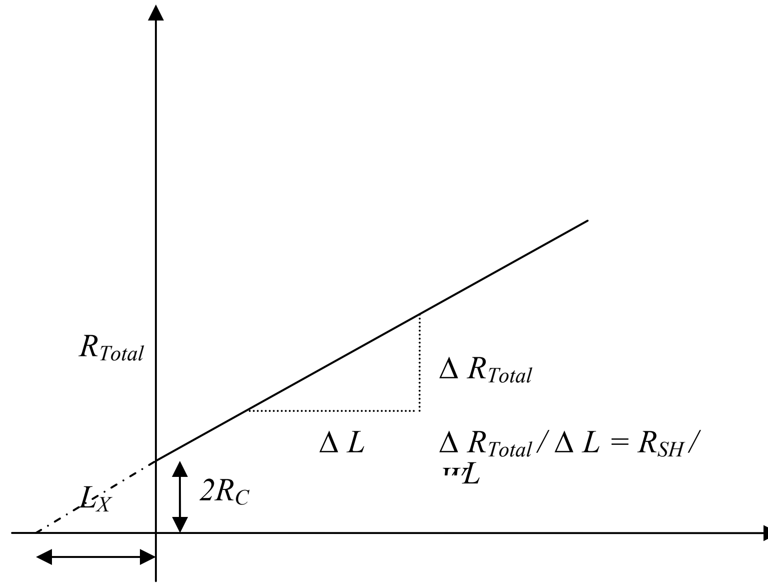

Fig. 5.3 Resistance vs. contact spacing, *L*, in the transmission line method.

Equation 5.3 is a straight line with a slope R_{SH} / W and a y-intercept of $2R_C$. By finding this line from a least squares fit to measurements of resistances as a function of contact spacing, the specific contact resistance of the metal-semiconductor interface and the sheet resistance of the semiconductor can be found. Another figure of merit in this graph is the so called "transfer length" L_T, which is defined as

$$L_T = \frac{L_X R_{SH}}{2R_{SK}}, \tag{5.4}$$

Where L_X is the x-intercept of the R_{Total} line, and R_{SK} is the sheet resistance of the semiconductor directly under the metal.

The significance of L_T is that it can be thought of as a length of the semiconductor underneath the metal having a resistance equal to the contact resistance R_C. This way, the total resistance R_{Total} can be thought of as being offered entirely by the semiconductor, R_C

being replaced by $\left(\frac{R_{Sk} L_T}{W}\right)$. If it is assumed that the metal pad length $S >> L_T$ then the specific contact resistance ρ_C is given by [29]

$$\rho_C = R_{SK}\, L_T^{\,2} \ . \tag{5.5}$$

Another assumption that is usually made is that $R_{SK} = R_{SH}$, which gives,

$$L_T = \frac{L_X}{2} \ . \tag{5.6}$$

$$\rho_C = R_{SH}\, L_T^{\,2} \, . \tag{5.7}$$

$$R_C = \frac{R_{SH} L_T}{W} \ . \tag{5.8}$$

From (5.7) and (5.8)

$$\rho_C = \frac{W^2 R_C^2}{R_{SH}} \ . \tag{5.9}$$

5.2 Sample preparation and measurement

Molybdenum (180 nm) was deposited on an undoped InAs substrate by electron-beam evaporation. A pattern was put on the molybdenum surface using photolithography and molybdenum was removed using CF_4/O_2 RIE to define the metal contacts. To define the TLM mesas, the sample was wet etched in the citric-acid-based etchant to a depth of ~500 nm. The width of the metal pads, W, was 100 µm and length S was 72 µm. The gap lengths L_I in the lithographic mask were 12, 14, 16, 18, 20, 24, and 28 µm. The actual gap lengths were measured after the fabrication process and were used to calculate the contact parameters.

A Micromanipulator-6000 probe-station, tungsten probes (2.4 µm diameter) and an HP3457A multimeter were used for the measurements. First it was verified that the contacts were ohmic by getting the *I-V* curves for the adjacent TLM pads using the Cascade Summit 11861 probe-station and Agilent 4155B semiconductor parameter analyzer. The TLM technique described was used to find the total resistance R_{Total} for the TLM pads, plotted against the corresponding gap length L_I. From the plot, the values of R_{SH} and R_C were found and Eq. (5.9) and Eq. (5.7) were used to calculate the values of the specific contact resistance, ρ_C, and the transfer length, L_T, respectively. The results are shown in Fig. 5.4. The two values of R_{Total} at each gap length in Fig. 5.4, Fig. 5.5 and Fig. 5.6 correspond to the measurements on two TLM patterns having the same gap lengths.

As seen from Fig. 5.4, the measured values of R_{Total} do not clearly follow a linear trend. Annealing the sample at temperatures at temperatures (250 ºC – 300 ºC) for different times (15–45 s) was tried to see if it would improve the linearity. The annealing was done in a Modular Pro RTP-600S rapid thermal processor in a nitrogen environment. No significant improvement was observed in the linearity of R_{Total}. One measurement of an annealed sample (290 ºC for 30 second) is shown in Fig. 5.5.

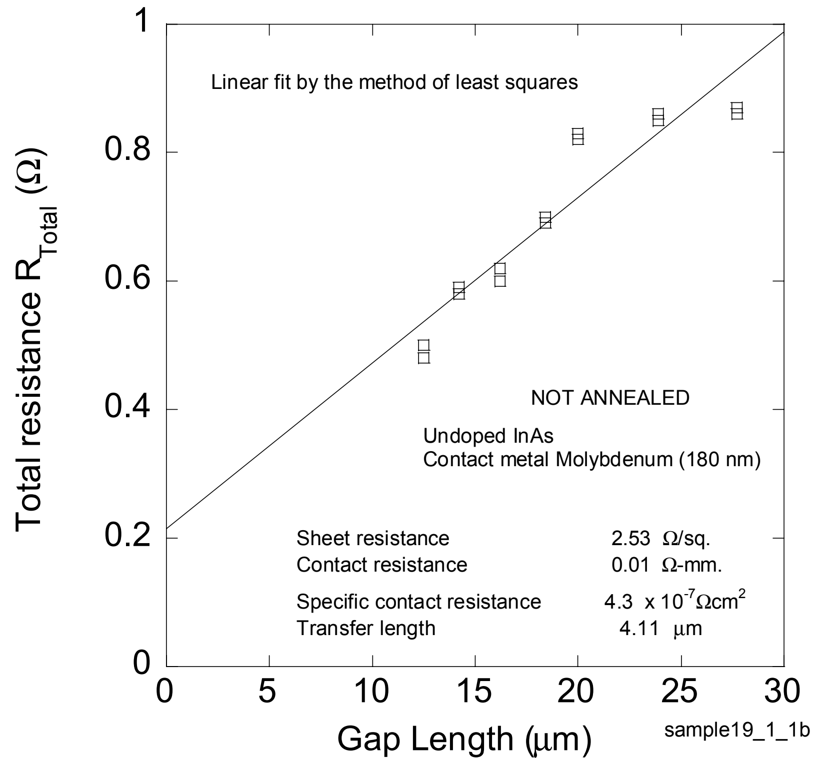

Fig. 5.4 Total resistance vs. gap length for an unannealed molybdenum-InAs contact

During this measurement as well as the measurement before annealing, a wide variation (up to 50 %) in the R_{Total} was noticed with the positioning of the four probes on the two adjacent metal pads. This suggests that the potential difference measured between the two metal pads varied with the positions at which they were measured, since the current supplied is invariant of the positioning of the probes. This suggested that the metal pads were not equipotential surfaces and there was a lateral resistance on the metal pad which resulted in potential variations across the pad. The TLM measurement technique assumes an equipotential metal pad surface.

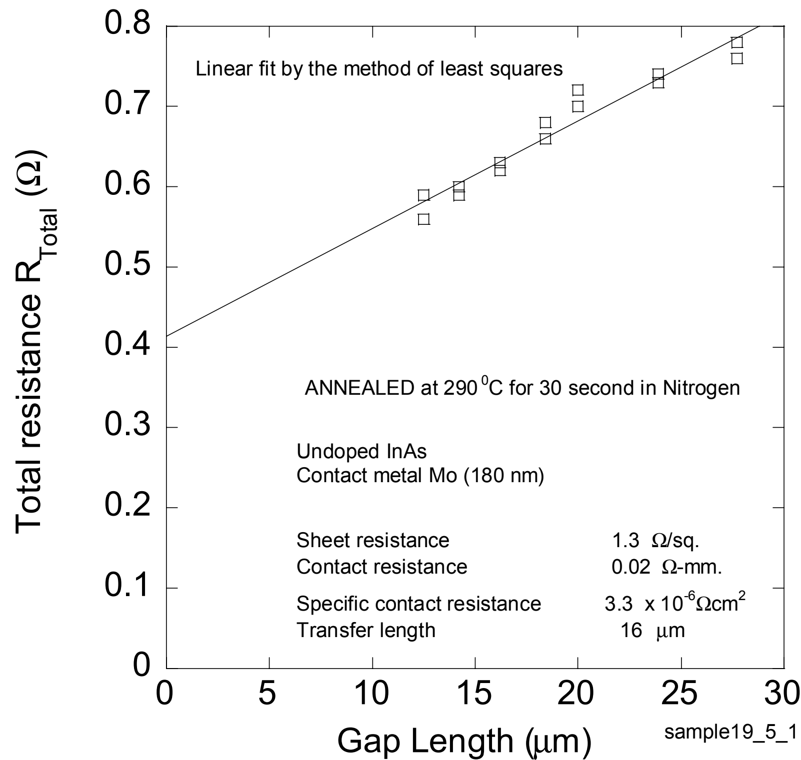

Fig. 5.5 Total resistance vs. gap length for molybdenum-InAs contact (after annealing).

Molybdenum has a low bulk resistivity of 5.14 µΩ-cm (for comparison, Au has a bulk resistivity of to 2.35µΩ-cm). However, the resistivity of a thin metal film can differ from its bulk value [30]. The resistivity of the molybdenum films deposited was measured to verify the effect of lateral resistance on the TLM measurement. To find the resistivity of the Mo films, the four point probe technique [31] was used. To constrain the current to flow within the molybdenum film, molybdenum was deposited on an insulating material (~300 nm of SiO_2 grown on silicon by wet oxidation). The molybdenum thickness was kept comparable to the thickness used in TLM measurements (~250 nm).

For purposes of comparison, a similar sample with gold (~ 300 nm on SiO_2) was also prepared.

The resistivity for gold was found to be 2.44 μΩ-cm, which is comparable to the bulk value. According to [30], the thin film resistivity of gold (electron-beam evaporated) is found to be 2.4 μΩ-cm, which compares well with this result. However, for molybdenum, the resistivity of the ~250 nm film was found to be 77.4 μΩ-cm, which is more than 12 times its bulk value. The resistivity of thin molybdenum films (sputtered) is reported to be 10 μΩ-cm [30]. Clearly in this case, the resistivity of the molybdenum film was much higher than the expected value, which is consistent with the hypothesis of potential variations across the metal pads in the TLM measurements.

To characterize the molybdenum-InAs contacts by the TLM technique, it was necessary to form an equipotential surface across the molybdenum pads. One way to achieve this is to deposit a highly conductive layer on top of the molybdenum pads which would ensure that the potential is the same across the metal pad. Gold was used as the metal to be put on molybdenum as gold is not likely to diffuse into molybdenum (In [32], the use of molybdenum as a diffusion barrier for gold in a Ti-Mo-Au system is reported). The metallization process was to: (a) evaporate molybdenum over the InAs surface, (b) create TLM patterns on molybdenum using photolithography, (c) evaporate gold and lift-off, (d) reactive ion etch the molybdenum using a CF_4/O_2 plasma with gold patterns as the mask, and (e) using photolithography, cover the TLM patterns with a photoresist etch-protect mask, define a TLM mesa by etching InAs in the citric acid etchant. Molybdenum (~230 nm) was deposited on undoped InAs. Metallization for the top contact metal was Ti/Pt/Au (10/10/200 nm). The TLM mesa height was 1.1 μm. The

width, W, and length, S, for the TLM pads were 97 and 72 µm respectively. The gap lengths were of 10, 12, 14, 16, 18, 22, and 26 µm. The actual lengths of the gaps were measured using an optical microscope (100x magnification) after the fabrication and were used to calculate the contact parameters.

As expected, the values of R_{Total} were now independent of the positioning of the probes on the metal pads. The results are provided in Fig. 5.6 and Fig. 5.7. Comparing these to the previous results with molybdenum contact pads, the variation of R_{Total} with gap lengths with Au/Mo metal pads seem to be more linear. However, the high values of the transfer length L_T obtained from the calculations cause a concern, since the equations used in calculating the contact parameters specifically assumed that, $S >> L_T$. However in this case, S and L_T calculated are comparable. One possible explanation for the high values of L_T could be the assumption of R_{SK} being equal to R_{SH} which sets the value of L_T to $\frac{L_X}{2}$. In many instances, it has been reported that the sheet resistance of the semiconductor underneath the metal R_{SK} is found to be significantly different from the semiconductor sheet resistance R_{SH} because of alloying/sintering effects [29].

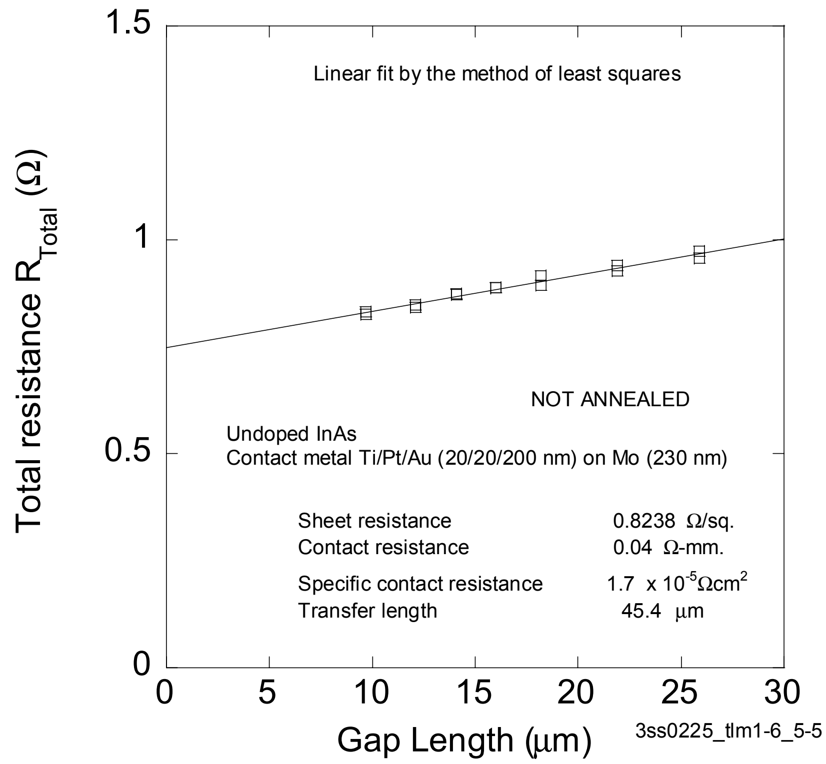

Fig. 5.6 Total resistance vs. gap length for an unannealed molybdenum-InAs contact with Ti/Pt/Au on top of molybdenum

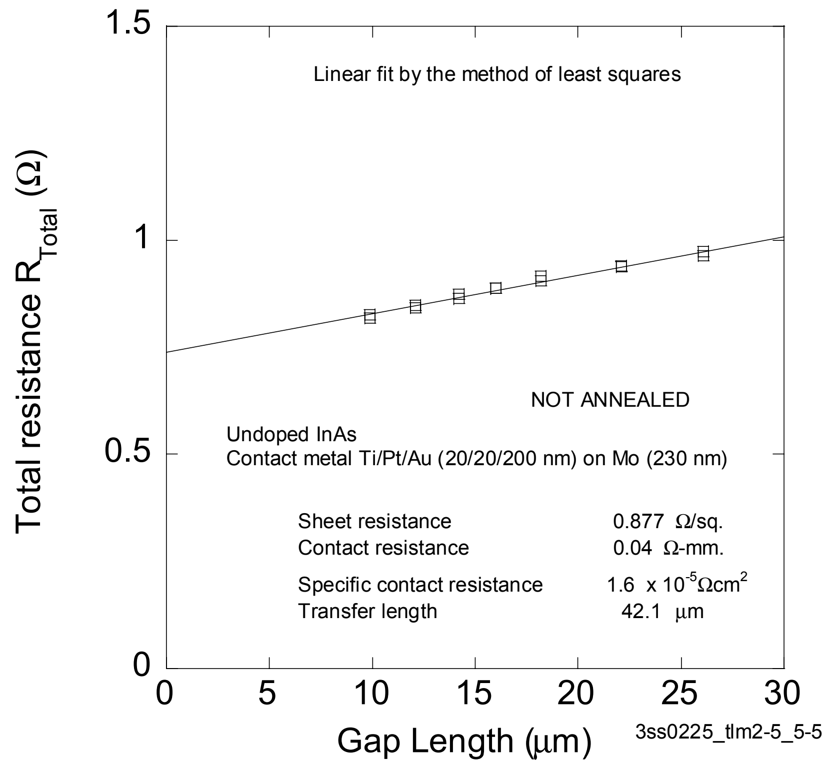

Fig. 5.7 Total resistance vs. gap length for an unannealed molybdenum-InAs contact with Ti/Pt/Au on top of molybdenum.

CHAPTER 6

BASE-COLLECTOR *P-N* JUNCTION STUDY

After designing the non-lift-off molybdenum metallization process and characterizing of the molybdenum-InAs contact, *p-n* junctions similar to those that might be used as the base-collector junction of HBTs, with molybdenum contact, were studied for the diode characteristics and its dependence on annealing. The quality of the molybdenum-InAs contact could also be estimated from the *I-V* characteristics.

6.1 Diode parameters

The ideal *I-V* characteristics for a p-n junction diode are given by [33]

$$J = J_s\left(e^{\left(qV/kT\right)} - 1\right) , \qquad (6.1)$$

where J is total current density, V is the potential difference across the junction, k is the Boltzman's constant and T is the operating temperature in Kelvin. This relation assumes: (a) the depletion layer is abrupt, (b) the electron and hole distributions are governed by Boltzman statistics, (c) the injected minority carrier concentration is small compared to the majority carrier concentration, and (d) no generation or recombination currents exist in the depletion region [34]. Deviations from ideal behaviors [35] can result from: (a) leakage currents on the surface (b) generation and recombination of carriers in the

depletion region, (c) intra-band tunneling of carriers through defect states in the bandgap, (d) high-level injection, and (d) effects of series resistance that alter the potential drop across the junction. In forward bias, recombination of carriers in the depletion region gives rise to a recombination current, J_{rec}, given by [36]

$$j_{rec} = \frac{qW}{2}\sigma v_{th} N_t n_i e^{\left(qV/2kT \right)} \quad , \tag{6.2}$$

where W is the width of the junction, σ is the hole and electron capture cross-section, v_{th} is the carrier thermal velocity, N_t is the trap density, and n_i is the intrinsic carrier concentration. The total forward bias current now can be given as

$$j_T = j_s\left(e^{qV/kT} - 1\right) + j_{rec} = j_s\left(e^{qV/kT} - 1\right) + \frac{qW}{2}\sigma v_{th} N_t n_i e^{\left(qV/2kT \right)} . \tag{6.3}$$

The I-V characteristics in the forward bias can thus be represented by an empirical formula [36]

$$j_F = Ce^{\left(\frac{qV_F}{\eta kT}\right)}, \tag{6.4}$$

where C is a constant and η is called the ideality factor, which is a number between 1 and 2. According to Eq. (6.3), when the diffusion current dominates the total diode current, η is 1 and when the diffusion current is dominated by the recombination current, η has the value 2.

If the diode current as given by Eq. (6.4) is plotted on a log scale against the voltage, we have, in the forward bias, for $V_F > 3kT/q$,

$$\log(j_F) = \log(C) + \frac{q}{\eta kT} V_F , \tag{6.5}$$

which is a straight line with slope $\frac{q}{\eta kT}$. At T = 300 K, and for η =1, the current increases by a decade per every 59.5 mV.

6.2 Wafer structure and fabrication process

Figure 6.1(a) shows the structure of the p-n diode (wafer R315). Figure 6.1(b) shows the equilibrium band diagram for the structure. Molybdenum (280 nm) was first deposited by electron-beam evaporation. Using photolithography and lift-off, Ti/Pt/Au (17/17/200 nm) metallization was used to define contacts on the molybdenum. Molybdenum was then reactive-ion-etched in a CF_4/O_2 plasma. A device mesa was defined by etching InAs to the InAs substrate in a citric acid based solution (discussed in Section 3.2.1). The devices were measured front-to-back, i.e. the back of the wafer is metallized with Ti/Pt/Au (20/20/200 nm) and used as the second contact for measurement. Figure 6.2 shows the device structure after fabrication.

Layer	Material	Type	Density cm^{-3}	Thickness nm
base	InAs	p+	1×10^{19}	50
collector	InAs	n	5×10^{16}	250
subcollector	InAs	n+	1×10^{19}	300
buffer	InAs	n	undoped	35
substrate	InAs	n+	$1\text{-}5 \times 10^{19}$	-

$As_2 = 2 \times 10^{-6}$ Torr, growth rate = 0.4 μm/hr

(a)

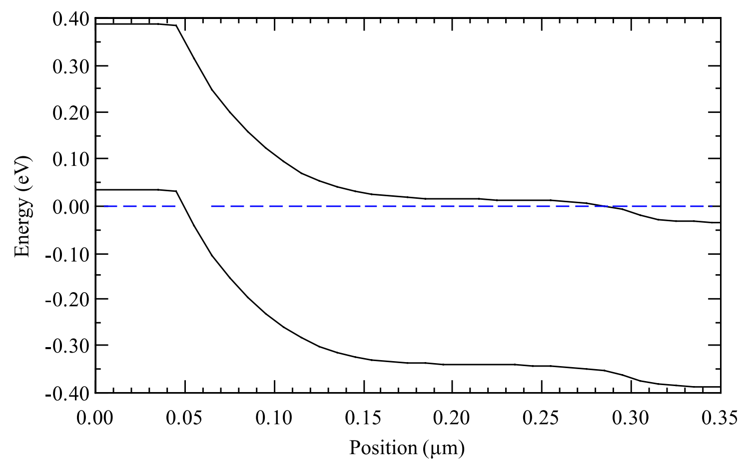

(b)

Fig. 6.1 *p*-n diode structure R315 grown by molecular beam epitaxy at Georgia Tech., Atlanta: (a) layer structure, (b) equilibrium energy band diagram (using the Poisson solver BandProf of W. R. Frensley).

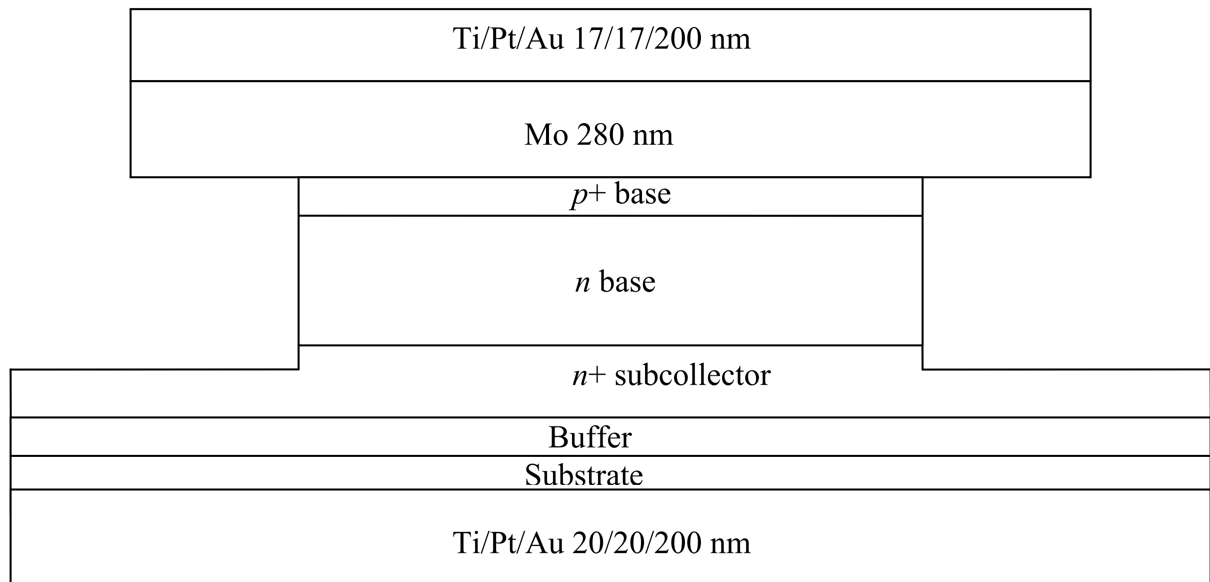

Fig. 6.2 Structure of a device made from the *p*-n diode structure R315.

6.3 Current-voltage (*I-V*) characteristics and analysis

The *p-n* junction characteristics were measured in the Cascade Microtech Summit-11861 probe-station using an Agilent 4155B semiconductor parameter analyzer. The measurement consisted of sweeping the applied voltage across the device through a range starting from reverse bias to forward bias. One electrical contact was made to the top metal of the device through a probe (Cascade Microtech coaxial probe of diameter 1 µm) and the second electrical contact was made through the wafer chuck. The devices measured were circular, with diameters of 15, 150, and 1500 µm. The *I-V* characteristics are shown in Fig. 6.3. Each device measured is labeled by a unique identifier.

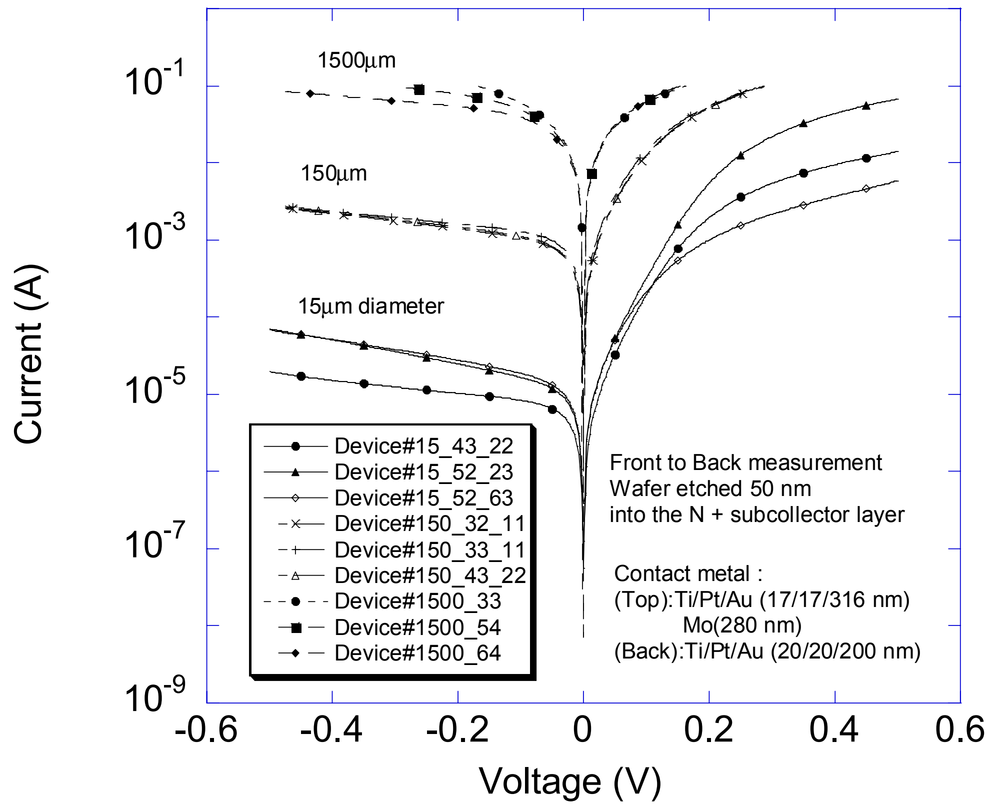

Fig. 6.3 Current-voltage (*I-V*) characteristics for the *p-n* structure devices (wafer R315) with molybdenum contact to the *p*+ layer.

Some non-uniformity can be seen in the diode characteristics in Fig. 6.3 for different devices of the same diameter. A significant series resistance (~50 Ω) is apparent, which depends on the probe pressure. The diode parameters for some devices shown in Fig. 6.3 are extracted in Table 6.1, using the same device identifier as in Fig. 6.3.

TABLE 6.1

DIODE PARAMETERS FOR THE *p-n* STRUCTURE DEVICES (WAFER R315)

WITH MOLYBDENUM CONTACT TO THE *p*+ LAYER

Device Identifier	Device Diameter (μm)	Ideality Factor η	Current Slope mV/decade
15_52_23	15	1.25	74.1
15_43_22	15	1.45	85.5
15_52_63	15	2.2	130.6
150_32_11	150	1.58	104.8
150_33_11	150	1.87	112.5
150_43_22	150	1.78	105.5

From Table 6.1, the measured ideality factors are all greater than one, suggesting a recombination current in the depletion region. For forward bias greater than 0.15 V, the log plot of the current is not linear. This appears to be due to the effect of series resistance which makes the potential difference across the junction different from the applied bias. From Fig. 6.3, the values of the series resistance for the devices 15_52_23, 15_43_22 and 15_52_63 were found to be 3.9, 21.7 and 56.9Ω respectively.

It is seen from Fig. 6.3 that the diode current does not scale with the device area for the three device sizes. This could be explained by the presence of a surface current component (section 2.3). The total current can be written as,

$$I_{Total} = J_D\left(\pi r^2\right) + J_S(2\pi r)\,, \tag{6.6}$$

where J_D is the current density in the bulk, J_S is the surface current density (cm^{-1}), and r is the radius of the device. Figure 6.4 (a) shows the dependence of the total current I_{Total} on the device diameter at different bias. From this curve, the values of J_D and J_S are extracted. Figure 6.4(b) shows the band diagram of InAs (p-type $N_a = 10^{19}$ cm^{-3}), with the Fermi level pinned 0.2 eV above the conduction band edge at the surface. From Fig. 6.4(b), the thickness of the surface accumulation layer, t, can be estimated to be 2.5 nm. We have,

$$\frac{J_S}{t} = n_S q \mu \frac{V}{l}\,, \tag{6.7}$$

where n_S is the electron density in the surface accumulation layer, q is the electronic charge, μ is the electron mobility, V is the potential across the device mesa and l is the height of the device mesa. Taking μ = 33000 cm^2/Vs [1], l =1 μm in Eq. 6.7, the value of n_S can be calculated. Table 6.2 lists the values of J_D, J_S, and n_S for different values of the applied bias.

The surface current density, $\frac{J_S}{t}$ (cm^{-2}) comes out to be $\sim 5\times10^4$ A/cm^2 for the bias range considered, which is quite high. This may be due to the low value (2.5 nm) of t used in the calculation. The electron density n_S has been assumed to be constant for the thickness t, which gives a low estimate for t. The electron density near the surface, n_S, has been found to be ~10^{16} cm^{-3}. The value for n_S from the BandProf program is 5×10^{15} cm^{-3}. This method could be used to measure the effectiveness of surface passivation schemes,

by comparing the surface current density (and surface electron density) for passivated and non-passivated samples.

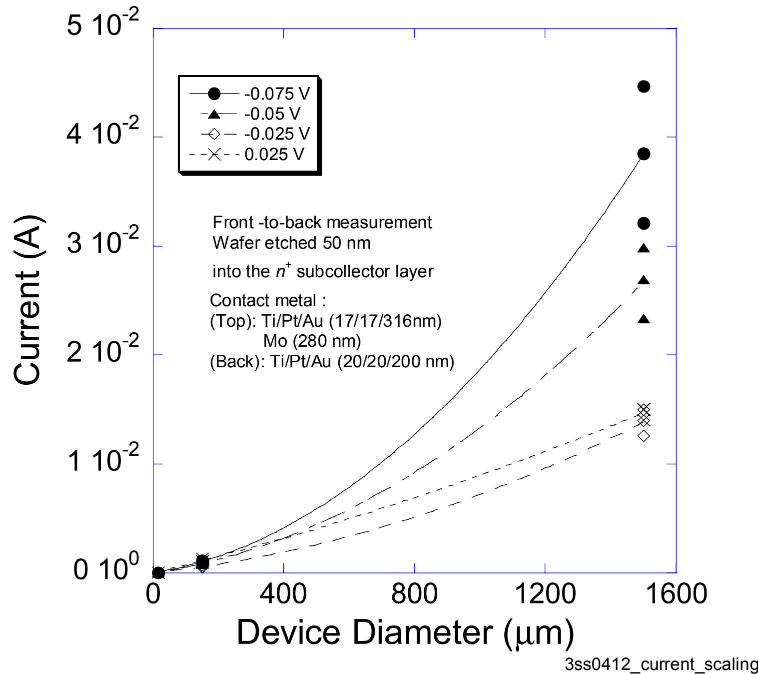

(a)

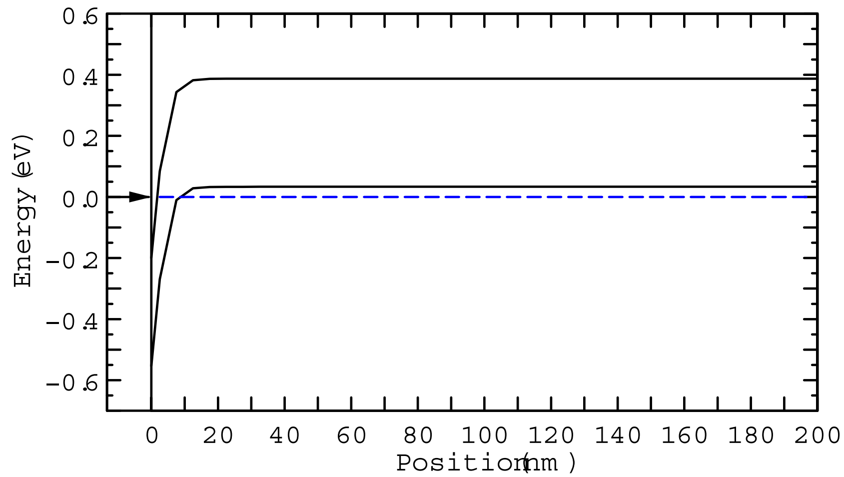

(b)

Fig. 6.4 (a) Dependence of the total current on the device diameter for the *p-n* structure devices (wafer R315) with molybdenum contact to the *p*+ layer, (b) Energy band diagram at equilibrium for InAs (*p*-type $N_a = 10^{19}$ cm^{-3}) showing the Fermi level pinning at the surface (using the Poisson solver BandProf program of W. R. Frensley).

TABLE 6.2

CURRENT DENSITIES AND THE SURFACE ELECTRON DENSITY AT DIFFERENT APPLIED BIAS

Applied Bias (*V*)	J_D (A/cm^2)	J_S (A/cm)	n_S (cm^{-3})
-0.075	1.77	1.53×10^{-2}	1.54×10^{16}
-0.05	1.14	1.4×10^{-2}	2.2×10^{16}
-0.025	0.52	1.01×10^{-2}	3.1×10^{16}
0.025	0.21	2.32×10^{-2}	7×10^{16}

6.4 Effect of annealing on the current-voltage characteristics

The *I-V* characteristics of the devices have been measured after temperature cycling from room temperature to 200 ºC. The temperature was controlled by a Temptronics TP03000 temperature controller on the Cascade 11861 probe station. The devices were measured in a nitrogen environment. Three elevated temperatures were chosen for the study, 100, 150 and 200 ºC. The devices were first measured at 25 ºC. The temperature was increased to 100 ºC, held for 15 minutes, and returned to 25 ºC. One set of devices were re-measured. The same procedure was repeated for two other sets of devices for temperatures 150 and 200 ºC respectively, and for the time indicated in Fig. 6.5. A representative curve is chosen from each of the three sets of devices. From Fig. 6.5, it's seen that in the reverse bias region, the current is increased with anneal. This could be

due to the degradation of the molybdenum-InAs contact. Increase in the surface current could be another explanation. In the forward bias characteristics, it can be seen that with anneal, the ideality factor for the device increases, which suggests an increase in the recombination current.

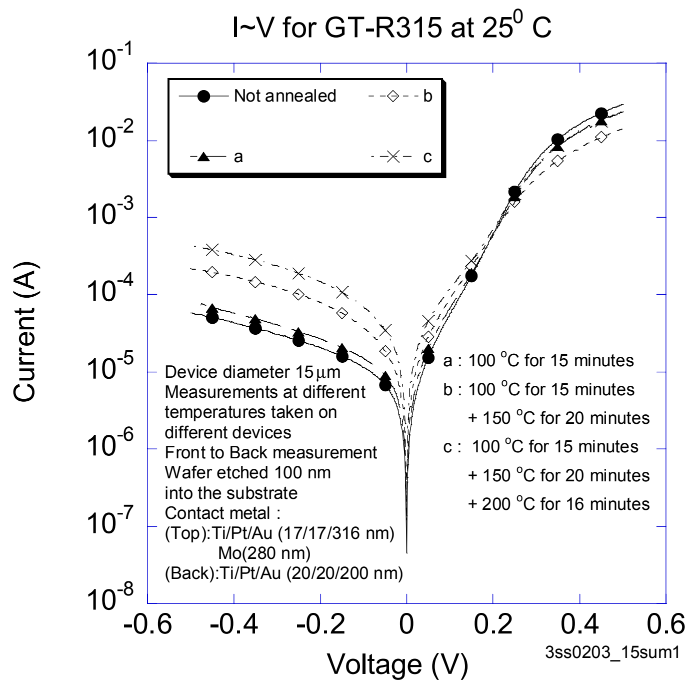

Fig. 6.5 Effect of annealing on the current-voltage (*I-V*) characteristics of the *p-n* diode structure (wafer R315) with molybdenum contact to the *p*+ layer.

Examination of wafer R315 in a Hitachi field emission scanning electron microscope (FESEM) shows that the citric acid undercuts the Mo contact isotropically, Fig. 6.6(a). It is also observed that probing can push the metal contact into contact with the subcollector, Fig 6.6(b). This may account for some of the *I-V* changes with probing pressure and placement. In Fig. 6.6(b), the impression of a central mesa, with a diameter

roughly one third of the device diameter, is also observed on the Mo/Ti/Pt/Au contact metal. At this point, no explanation for this feature is available, but it is observed on all the 15 µm diameter devices.

(a)

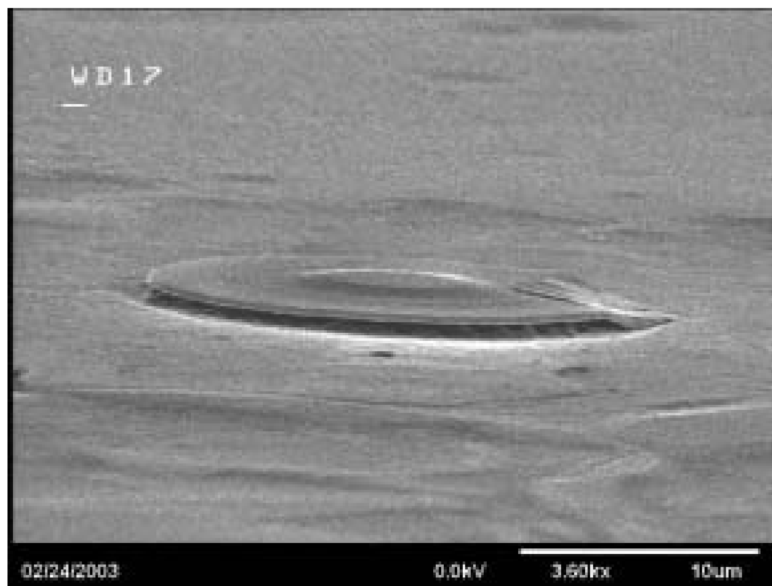

(b)

Fig. 6.6 Scanning electron microscope images of the *p-n* diode structure (wafer R315) after annealing, (a) an unprobed device, (b) a probed device having non-rectifying current-voltage (*I-V*) characteristics.

CHAPTER 7

CONCLUSION

Etching and metallization processes for InAs-base HBTs have been developed. Of the five etchants studied for selective etching of InAsP over InAs, only the phosphoric acid based etchant etches InAsP faster than InAs, with a selectivity less than 2. A process for molybdenum contact formation on InAs has been developed including etching processes for molybdenum. Of the molybdenum etchants studied, three etchants have been found to be useful for the purpose, (a) H_2O_2, (b) 15 NH_4OH: 10 H_2O_2: 100 H_2O, and (c) reactive ion etching in CF_4/O_2. With the first two wet-chemical etchants, however, etching for times longer than 3 minutes with AZ5214E photoresist as the etch mask results in etching of molybdenum under the etch mask. This can be prevented by using a different etch mask like SiO_2. Due to the effects of high resistivity of thin molybdenum films (77.4 μΩ-cm), a gold layer is added on the top of molybdenum. The properties of the base-collector *p-n* junction of the HBT structure with molybdenum contact have been studied. The lowest value of the ideality factor found from the *I-V* characteristics 1.25. Some degradation of the molybdenum-InAs contact due to annealing is seen with an apparent increase in the reverse saturation current of the *p-n* junction. Molybdenum/InAs contacts are undercut in citric acid etchants suggesting that InAs dry etchants are needed.

APPENDIX

PROCESS TRAVELER FOR INDIUM ARSENIDE *P-N* DIODE WITH MOLYBDENUM CONTACT

Solvent clean
Starting Date Time

1. Cleave a sample
2. Blow sample with N_2 gun to remove particles
3. Prepare acetone and methanol.
4. Soak the sample in hot acetone for 5 min.
5. Transfer the sample to hot methanol for 5 min.
6. Spray the sample with methanol and blow dry with a N_2 gun.
7. Hot plate dry the sample for 10 seconds.

Molybdenum deposition

1. Load the sample into the evaporator.
   Roughing time ____________ min
   Cryopump time ____________ min
   Base pressure _______ Torr
2. Molybdenum thickness ____
   Deposition rate

Comments
End Time

Photolithography for top-metal deposition
Starting Date Time

Before continuing fabrication, solvent cleaning may be required if the fabrication process has been paused over a day.

1. Turn on Karl Suss aligner.
2. Spin AZ 5214E at 5000 RPM for 30 s (about 1.3 μm of photoresist)
3. Soft bake in the hot plate for 1 minute at 90 ˚C.
4. Measure the Karl Suss lamp intensity , measured value is ____________________ mW/cm^2
5. Edge removal (if the sample dimensions are less that 1 cm).
   a) Soft Contact mode.

b) Expose for 2100 mJ/cm^2 with an edge-removal mask. (exposure time ____s)
c) Develop for 30 s in AZ 327 MIF. Rinse in DI water and blow dry in N_2.
d) Switch the grip to another edge on sample and develop for additional 30 s
e) Check the edge in a microscope.
f) Use acetone-soaked microswab to remove the PR residue (if any).

6. Align the sample in Karl Suss with the ______________________ mask.
7. Primary expose for 80 mJ/cm^2 in ST mode. (Time = ____________ s)
8. Image-reversal-bake the sample at 120˚C for 60 s.
9. Flood expose for 220 mJ/cm^2 in soft contact mode. (Time = ____________ s)
10. Develop for 35 s in AZ 327 MIF. Rinse the sample in DI water and blow dry in N_2. Check the pattern transfer with the microscope. Alignment marks should look clean.
11. Load the sample into the evaporator.
    Roughing time __________ min
    Cryopump time _________ min
    Base pressure ___________ Torr
13. Evaporate

Metal	Thickness (Å)

14. Lift-off the PR in warm acetone. Rinse the sample in methanol and blow dry in N_2.
15. Examine the sample in microscope. Alignment marks should be well defined.

Comments
End Time

Molybdenum etching
Starting Date Time

Before continuing fabrication, solvent cleaning may be required if the fabrication process has been paused over a day.

1. Check the RIE log. If SF_6 has been the gas used last, then do an Oxygen cleaning process for 30 minutes (till the plasma color changes to beige).
2. Load the sample into the RIE chamber.
3. Condition the chamber with CF_4/O_2 for 2 minutes.
4. RIE etch for the desired depth with the recipe (etch rate = 1.8 nm/s)
    a. CF_4 26 sccm
    b. O_2 5 sccm
    c. Pressure 60 mT
    d. Power 100 W
    Record the DC bias _______________ V
5. Take the sample out and inspect it. The Brown color of Molybdenum should be gone and InAs below should be visible (if not, then RIE for longer time).
6. If the brown film doesn't go with RIE, remove it with H_2O_2 (10 s) or H_2O: HCl (10:1) (10 s).

7. Measure the total metal height and verify this with the expected value (Mo + Top Metal).
   Metal height ____

Comments
End Time

Device Mesa etching
Starting Date Time

Before continuing fabrication, solvent cleaning may be required if the fabrication process has been paused over a day.

1. Etchant Citric acid based etchant

Etch Time Etch Depth

Comments
End Time

Back metal deposition
Starting Date Time

Before continuing fabrication, solvent cleaning may be required if the fabrication process has been paused over a day.

1. Spin AZ 5214E at 2000 RPM for 30 seconds.
2. Soft bake on the hot plate for 1 minute at 90˚C.
3. Load the sample in the evaporator with the back of the wafer exposed to evaporation.
   Roughing time __________ min
   Cryopump time _________ min
   Base pressure ___________ Torr.
5. Evaporate

Metal	Thickness (Å)

4. Remove PR with acetone. Rinse the sample in methanol and blow dry in N_2.

Comments
End Time

REFERENCES

[1] K. Brennan and A. Brown, *Theory of Modern Electronic Semiconductor Devices*, John Wiley & Sons, 2002, page 437.

[2] A. Seabaugh and Qingmin Liu , private communication.

[3] J. –S. Rieh, B. Jagannathan, H. Chen, K. T. Schonenberg, D. Angell, A. Chinthakindi, J. Florkey, F. Golan, D. Greenberg, S. –J. Jeng, M. Khater, F. Pagette, C. Schnabel, P. Smith, A. Stricker, K. Vaed, R. Volant, D. Ahlgren, G. reeman, K. Stein, and S. Subbanna, "SiGe HBTs with Cut-Off Frequency of 350 Hz," *IEEE IEDM Technical Digest*, 2002, pp. 771-774.

[4] D. A. Sunderland and P. D. Dapkus, "Optimizing N-p-n and P-n-p Heterojunction Bipolar Transistor for Speed," *IEEE Transactions on Electron Devices*, ED-34, 1987, pp. 367-377.

[5] D. H. Chow, HRL Laboratories, CA, private communication.

[6] S.M. Sze, *Physics of Semiconductor Devices,* 2nd edition, John Wiley and Sons, 1999, page 140.

[7] S. M. Sze, page 141.

[8] S. M. Sze, page 158.

[9] K. Brennan and A. Brown, page 154.

[10] K. Brennan and A. Brown, page 144.

[11] K. Brennan and A. Brown, page 150.

[12] H. Kroemer, "Heterostructure bipolar transistors and integrated circuits," *Proceedings of the IEEE,* vol. 70, 1982, pp. 13-25.

[13] J.Tang, and K. Hess, "Investigation of transient and electronic transport in GaAs following high energy injection," *IEEE Transactions on Electronic Devices,* ED-29, 1982, pp. 1906-10.

[14] K. Brennan, and K. Hess, "Transient electronic transport in staircase heterostructures," *IEEE Electron Devices Letters,* EDL-4, 1983, pp. 419-21.

[15] D. C. Tsui, "Observation of surface bound state and two-dimensional energy band by electron tunneling," *Physical Review Letters,* vol. 24, 1970, pp. 303-306.

[16] L. Canali, J. Wildoer, O. Kerkhof, and L. P. Kouwenhoven, "Low- termperature STM on InAs(110) accumulation surfaces," *Applied Physics A*, 66, 1998, pp. S113-S116.

[17] J. Matthews and A. Blakeslee, "Defects in epitaxial multilayers," *Journal of Crystal Growth*, vol.27, 1974, pp. 118-125.

[18] P. Elias, V. Cambel, S. Hasenohrl, P. Hudek, and J. Novak, "SEM and AFM characterization of high-mesa patterned InP substrates prepared by wet etching," *Materials Science and Engineering*, B66, 1999, pp. 15-20.

[19] Sadao Adachi and Hitoshi Kawaguchi, "Chemical etching characteristics of (001)InP," *Journal of the Electrochemical Society*, vol. 128, no. 6, 1981, pp. 1342-1349.

[20] K. Akita, T. Kusunoki, S. Komiya and T. Kotani, "Observation of etch pits produced in InP by new etchants," *Journal of Crystal Growth*, 46, 1979, pp. 783-787.

[21] T.E. Tietz and J.W. Wilson, *Behavior and Properties of Refractory Materials*, Stanford University Press, 1965, page 1.

[22] *CRC Handbook of Materials Science and Engineering*, CRC Press, 2001, page 213.

[23] L. Northcott, *Molybdenum*, Butterworths Scientific Publications, London, 1966, page 23.

[24] L. Northcott, page 29.

[25] R. Allen, M. Foster and T. Yen, "Deep U.V. hardening of positive photoresist patterns," *Journal of the Electrochemical Society*, vol. 129, no. 6, 1982, pp. 1379-1381.

[26] A. Zambova, L. Zambov, and K. Stantchev, "Mechanism and kinetics of molybdenum films etching in peroxide-ammonia Solution," *Journal of the Electrochemical Society,* vol. 139, no. 9, 1992, pp. 2470-2477.

[27] R.J. Saia and B. Gorowitz, "The reactive ion etching of molybdenum and bilayer metallization systems containing molybdenum," *Journal of the Electrochemical Society*, vol 135, no. 11, 1988, pp. 2795-2802.

[28] W. Shockley, "Research and investigation of inverse epitaxial UHF power transistors," *Report No. Al-TOR-64-207*. Air Force Atomic Laboratory, Wright-Patterson Air Force Base, 1964.

[29] G.K. Reeves, H.B. Harrison, "Obtaining the specific contact resistance from transmission line model measurements," *IEEE Electron Device Letters*, vol. EDL-3, no. 5, 1982, pp. 111-113.

[30] S. O. Kasap, *Principles of Electronic Materials and Devices,* 2nd Edition, McGraw-Hill, 2002, page 153.

[31] L.B. Valdes, "Resistivity measurements on germanium for transistors," *Proceedings of the I.R.E*, 1954, pp. 420-427.

[32] Y. Kitaura, T. Hashimoto, T. Inoue, K. Ishida and N. Uchitomi, "Long-term reliability of Pt and Mo diffusion in Ti-Pt-Au and Ti-Mo-Au metallization systems for GaAs digital Integrated circuits," *Journal of Vacuum Science and Technology B,* vol. 12, no. 5, 1994, pp. 2985-2991.

[33] S. M. Sze, page 87.

[34] S. M. Sze, page 84.

[35] S. M. Sze, page 90.

[36] S. M. Sze, page 92.